RSC Advances

ROYAL SOCIETY OF CHEMISTRY

PAPER

View Article Online
View Journal | View Issue

Cite this: *RSC Adv.*, 2026, **16**, 27397

Enhancement of photovoltaic and thermoelectric properties of A-site doped $A_{3-x}A'_xIO$ (A/A′=K, Rb, Cs) anti-perovskites with room temperature phonon stabilization: a DFT and molecular dynamics study

Kashfi Uddin and Abu Sadat Md. Sayem Rahman *

In this work, alkali-metal A-site-doped $A_{3-x}A'_xIO$ (A/A′ = K, Rb, Cs) anti-perovskites are systematically investigated using Density Functional Theory (DFT) and Molecular Dynamics (MD) simulations. The structural, mechanical, thermal, electronic, optical, and thermoelectric properties are analyzed using DFT, while MD & *Ab initio* MD simulations are employed to examine anharmonic lattice stabilization and thermal stability, respectively, at room temperature. The effect of larger alkali-metal substitution is analyzed for three pristine cubic anti-perovskites (K_3IO, Rb_3IO, and Cs_3IO), and for 33.33% and 66.67% A-site doping in six tetragonal anti-perovskites (K_2CsIO, KCs_2IO, K_2RbIO, KRb_2IO, Rb_2CsIO and $RbCs_2IO$). A-site doping results in bandgap narrowing and bowing, with reduced direct band gaps in the ranges 0.33–0.61 eV (GGA-PBE), 0.53–0.74 eV (GGA-RPBE), and 1.41–1.67 eV (HSE06). It leads to enhanced optical absorption (0.4–0.5 $\times$ 10^5 cm^{-1}) in the visible spectrum region. Notably, in terms of thermoelectric efficiency, KRb_2IO and K_2CsIO exhibit the highest *ZT* values of 0.5–0.6, at their melting point (T_m ~490 K). At higher temperatures, K_2CsIO achieves the highest PF of 7 $\times$ 10^{11} W K^{-2} m^{-1} s^{-1}. All compounds are mechanically and thermodynamically stable. At 0 K, Cs_3IO, KRb_2IO and $RbCs_2IO$ show negative phonon modes, indicating dynamical instability. However, at 300 K, MD simulations stabilize all phonon modes through anharmonic phonon renormalization, which is further validated by the Dulong–Petit limit. The doped phases also show improved Shockley–Queisser limit efficiency, ductility and machinability. These results establish A-site-doped non-toxic anti-perovskites as promising candidates for photovoltaic and thermoelectric applications, while also demonstrating MD to be an effective method for assessing room temperature dynamic stabilization.

Received 16th February 2026
Accepted 1st May 2026

DOI: 10.1039/d6ra01390b

rsc.li/rsc-advances

1 Introduction

Photovoltaic energy is being recognized as a major player in the future of energy technologies. Perovskite-related compounds are one of the important materials in photovoltaics (PVs). There has been an intensive interest in enhancing their photovoltaic properties by modifying their structures, together with new doping schemes. The photovoltaic performance of single-junction perovskite solar cells (PSCs) has developed dramatically, from less than 4% power conversion efficiency (PCE) in 2009 to more than 26.95% in the latest reports.[1,2] This progress has been linked to a combination of long carrier diffusion lengths, low exciton binding energies, strong optical absorption, tunable band gaps, and high defect tolerance.[3] As a result, perovskite materials are now being seen as viable candidates for a wide variety of optoelectronic and energy applications. Over the last decade, mixed A-site cation and halide organic-inorganic perovskites have been demonstrated to exhibit superior performance over their single-cation counterparts in both efficiency and operational stability. A-site cation mixing has been correlated with higher photovoltaic efficiencies, improved stability against degradation by light, heat and/or moisture, and increased versatility in band-gap tuning.[4] The major benefit of mixed-cation systems is the ability to tailor electronic and optical properties. Up to now, the highest efficiency of single-junction mixed-cation compositional PSC (Cs/FA mixed compositions) reported is 26.97%.[5]

Traditional halide perovskites have historically received most of the attention in terms of new materials to be used in photovoltaic applications because of their semiconducting properties. While nowadays, there is currently an increasing amount of research focused upon another type of perovskite material called the anti-perovskite, which has an inverted ionic configuration A_3BX. Here, the anion occupies the central

Department of Materials and Metallurgical Engineering (MME), Chittagong University of Engineering & Technology (CUET), Chittagong-4349, Bangladesh. E-mail: mdsayem@cuet.ac.bd; Tel: +880 1318503244

octahedral site, and the cations form the surrounding lattice framework.[6] Due to their relatively unique structural properties, like a wide range of compositional options (due to substitution), and flexibility in structural relationships with other materials, anti-perovskites show great potential for several applications, such as thermoelectric devices, batteries, and energy-storage systems.[7] For instance, chemical substitution and compositional tuning further expand the functional scope of anti-perovskites. Notably, K_3CuO, K_3AgO, Ca_3PbS, Sr_3PbS, Ba_3PbS, K_4OBr_2, K_4OI_2, Ca_6NFSn_2, and Sr_6NFSn_2 have been reported to exhibit promising thermoelectric figures of merit (*ZT*), ranging from 0.7 to 1.5 at different temperatures.[8,9] Ge doping in Mn_3AN (A = Cu, Zn, Ga) systems has achieved a pronounced negative thermal expansion coefficient.[10] K_3AuO possesses exceptionally low thermal conductivity and high carrier concentration, indicating its potential for TE device applications.[11] At room temperature, Ca_3XO (X = Pb, Sn) compounds have shown excellent thermoelectric (TE) power generation performance.[11] Mg_3BO (B = Si, Ge, Sn, Pb) maintained narrow direct band gaps (<0.5 eV), making them suitable for IR detection and thermoelectric applications.[12] Besides these, Cs_3BrO and Rb_3BrO are considered as top candidates for lead-free, high-performance solar absorbers.[13] Nitride-based anti-perovskites, such as Ca_3BN (B = P, As, Sb, and Bi), possess direct band gaps and high optical absorption coefficients, as well as tangible thermoelectric performance.[14] $(Li/Na/K)_3OI$ reveals strong light absorption as a promising candidate for perovskite solar cell applications.[12] These favourable structural and electronic features make anti-perovskites promising candidates for next-generation, high-performance solar-cell absorbers and thermoelectric operations.

Beyond these, compositional tuning through chemical doping greatly impacts the thermoelectric properties of perovskite compounds. Vijay *et al.* synthesized A-site doped derivative of $CaMnO_3$ ($La_{0.1}Ca_{0.9}MnO_3$), which achieves the highest *ZT* of ~0.13 at 1073 K.[15] Additionally, Torres *et al.* synthesized $Ca_{1-x}La_xMn_{1-y}Nb_yO_3$ ceramics ($x = 0$ or 0.1; $y = 0$ or 0.02), where La^{3+}-doped (on A-site) and Nb^{5+}-doped (on B-site) $CaMnO_3$ ceramics displayed the highest electrical conductivity and the highest Seebeck coefficient, respectively.[16] Amirkhizi *et al.* has found PF of 0.47 mW (K^{-2} m^{-1}), and 0.25 *ZT* at 800 °C for A-site co-doped $Ca_{0.98}Y_{0.01}La_{0.01}MnO_3$ synthesized sample.[17] Park *et al.* achieved the *ZT* value of 0.16, 0.17 and 0.24, respectively, for synthesized B-site doped $SrTi_{0.95}Nb_{0.05}O_3$, A-site doped $Sr_{0.95}Dy_{0.05}TiO_3$, and both AB-site co-doped $Sr_{0.95}Dy_{0.05}Ti_{0.95}Nb_{0.05}O_3$ at 600 °C.[18] Wu *et al.* synthesized A-site doped Pr_2CoFeO_6 sample ($Pr_{0.8}Sr_{0.2}CoFeO_6$), which significantly improved *ZT* by 233%, from 0.015 (773 K) to 0.05 (673 K),[19] through enhancing the carrier concentration and PF. Similarly, Zhang *et al.* synthesized Yb-La-Nb-doped $SrTiO_3$ sample (at an doping ratio of $La_8Yb_2Nb_{15}$), which achieved the largest PF value of 0.9 mW m^{-1} K^{-2} and a low thermal conductivity of 2.9 W m^{-1} K^{-1}, resulting in a high *ZT* value of 0.32 at 1000 K.[20] Shah *et al.* theoretically investigated that *ZT* increases with increasing Bi content at the B-site and are found to be 0.93, 0.94 and 0.95 for $Cs_2AgSc_{1-x}Bi_xBr_6$ ($x = 0$, 0.25 and 0.5).[21]

Beyond thermoelectric, perovskites also demonstrate significant potential in solar applications due to their tunable photovoltaic properties. Firdous *et al.* numerically investigated that A-site doping in La_2NiMn0_6 with Sr and Eu reduced the band gap from 1.2 to 1 eV and 0.9 eV, respectively, which increases the absorption value from 1 to 1.4 (arbitrary unit) within the visible range.[22] Jung *et al.* synthesized B-site doped $CsSn_{0.96}Zn_{0.04}Br_3$ PSC, which achieved 2.59% PCE.[23] Shah *et al.* theoretically showed that the reduction in band gap from 2.72 to 1.55 eV leads to enhancement in absorption peaks in the visible range by Bi doping at the B-site of $Cs_2AgSc_{1-x}Bi_xBr_6$ ($x = 0$, 0.25 and 0.5) perovskite, favouring the solar cell performance.[21] Gahlawat *et al.* theoretically showed that B-site doping in $Ba(Hf_{1-x}Zr_x)S_3$ perovskite alloys achieves PCE of 25.15% for $x = 0.75$.[24] Hossain *et al.* numerically show that sulfur doping (X-site) at $BaZrO_{3-x}S_x$ reduced the bandgap from 4.235 eV in $BaZrO_3$ to 1.197 eV in $BaZrS_3$, while $BaZrOS_2$ shows a 1.896 eV direct bandgap,[25] which makes it especially interesting for optoelectronic applications. Huang *et al.* numerically show that X-site doping in $CsGeBr_{3-x}I_x$ exhibits high optical absorption coefficients of (5.06–5.78) × 10^5 cm^{-1} within the visible spectrum.[26]

Overall, extensive research has been conducted on A-site-doped perovskites for thermoelectric applications, owing to their excellent tunability. On the other hand, both B and X-site-doped perovskites have been explored extensively for solar applications due to their narrow band gap and carrier modulation. But dopant elements used in both applications, like Lanthanum (La), Dysprosium (Dy), Praseodymium (Pr), Europium (Eu) and Ytterbium (Yb) are subject to volatile supply chains and high extraction costs.[27] Similarly, Niobium (Nb) and Cobalt (Co) are increasingly expensive due to competition with the battery and aerospace industries.[28,29] Moreover, conventional oxide perovskites ($CaMnO_3$, $SrTiO_3$) often require extremely high sintering temperatures (often >1300 °C) to achieve the density necessary for high electrical conductivity.[16,30] This energy-intensive manufacturing process of the thermoelectric device increases the carbon emissions. Regarding this, non-toxic alkali metals can minimise both the scarcity problem and high-temperature manufacturing costs as they are more abundant in earth crust with comparatively lower melting points. But there is very few work on alkali site-doped anti-perovskites, especially dedicated to thermoelectric and photovoltaic applications. Considering these research gaps, A-site-doping with alkali metals in $A_{3-x}A'_xIO$ (A/A′ = K, Rb, Cs) anti-perovskites has been investigated in this work. The pristine compounds K_3IO, Rb_3IO and Cs_3IO have been synthesized in the experiment,[31–33] *via* solid-state reaction of equimolar amounts of alkali metal halides and alkali metal oxides. However, a detailed theoretical investigation of the electronic, mechanical, thermal, optical, and thermoelectric properties is largely absent in the experimental studies reported by Feldmann *et al.*[31] This research gap has been addressed comprehensively in this work along with A-site doping with alkali metals K, Rb and Cs. The primary objective of this work is to examine the feasibility of $A_{3-x}A'_xIO$ (A/A′ = K, Rb, Cs) anti-perovskites for thermoelectric and photovoltaic applications

by enhancing the functional properties. With this aim, 33.33% and 66.67% Cs doping is introduced into both K_3IO and Rb_3IO, leading to the formation of K_2CsIO, KCs_2IO, Rb_2CsIO, and $RbCs_2IO$. In addition, 33.33% and 66.67% Rb doping is applied to K_3IO, resulting in anti-perovskites K_2RbIO and KRb_2IO, respectively. A comparative analysis of these six doped compounds, together with the three pristine phases (K_3IO, Rb_3IO, and Cs_3IO), reveals a wide range of tunable properties with strong potential for optoelectronic and thermoelectric applications.

2 Computational methodology

The functional properties of the anti-perovskite $A_{3-x}A'_xIO$ (A/A′ = K, Rb, Cs) compounds have been calculated using first-principles density functional theory with the Quantum ESPRESSO (QE) package.[34] All simulations have been performed using the plane-wave pseudopotential method with ultrasoft pseudopotentials.[35] Here the valence electron configurations are K: $3s^23p^64s^1$, Rb: $4s^24p^65s^1$, Cs: $5s^25p^66s^1$, O: $2s^22p^4$, and I: $5s^25p^5$. The exchange-correlation effects among the valence electrons have been treated with the Perdew–Burke–Ernzerhof (PBE)[36] functional within the generalised gradient approximation (GGA).[37] The GGA-PBE functional is used for evaluating the structural, mechanical and dynamic properties. Although the PBE functional reliably predicts lattice parameters and total energies, it shows clear limitations in accurately describing electronic properties, particularly the band gap. To address these shortcomings, the revised Perdew–Burke–Ernzerhof (RPBE),[38] and hybrid Heyd–Scuseria–Ernzerhof (HSE06)[39] functionals have been employed. The RPBE is a slight revision of the PBE functional, which systematically improves the atomization energies of small molecules. The HSE06 functional is recognized as a highly efficient and reliable approach for predicting electronic and optical properties, as it incorporates a fraction of exact exchange and significantly improves band-gap accuracy.

The ground state total energy is evaluated as a function of volume during the simulation of $A_{3-x}A'_xIO$ (A/A′ = K, Rb, Cs) compounds. The crystal structures are then optimised geometrically through variable-cell relaxation. This procedure follows the Birch–Murnaghan equation, as expressed:[40,41]

$$E(V) = E_0 + \frac{9V_0B_0}{16}\left\{\left[\left(\frac{V_0}{V}\right)^{\frac{2}{3}} - 1\right]^3 B_0 + \left[\left(\frac{V_0}{V}\right)^{\frac{2}{3}} - 1\right]^2 \left[6 - 4\left(\frac{V_0}{V}\right)^{\frac{2}{3}}\right]\right\} \quad (1)$$

where E_0 and V_0 are the ground-state energy and corresponding ground-state volume of the system. In the self-consistent field calculations, a $6 \times 6 \times 6$ k-point mesh is used. The optimised lattice parameters are then utilized in non-self-consistent calculations with a denser $12 \times 12 \times 12$ mesh. The plane-wave total energy convergence threshold has been maintained at 10^{-8} Ry. The VESTA (Visualization for Electronic and Structural Analysis)[42] package is used to visualise the unit cell and the corresponding charge density mapping.

To assess the chemical stability of the anti-perovskites, their formation energies are calculated using the following equation:[43]

$$\Delta E_f = \frac{E_{tot}(\text{compound}) - E(\text{I}) - E(\text{O}) - mE\left(\text{A} - nE\left(\text{A}'\right)\right)}{5} \quad (2)$$

Here, the total energy of the compound's unit cell is denoted as E_{tot}(compound), while the atomic energies of I, O, and A/A′ (A/A′ = K, Rb, Cs) are denoted as E(I), E(O), E(A), and E(A′), respectively, where m and n represent the number of A/A′ site atoms.

The phonon dispersion at 0 K has been investigated using density functional perturbation theory (DFPT).[44] After that, phonon properties at 300 K are evaluated through the temperature-dependent effective potential (TDEP)[45] approach combined with molecular dynamics (MD).[46] This allows a detailed investigation of the dynamical stability of the studied compounds. After equilibration, atomic positions and forces are recorded at regular intervals, which provide the dataset for the TDEP fitting. In the TDEP method, temperature-dependent force constants are extracted by fitting a harmonic model along the MD trajectory. A large set of uncorrelated snapshots is used to ensure statistical accuracy. The procedure yields second-order interatomic force constants of the system at 300 K. These are employed to construct dynamical matrices on a dense q-point grid within the primitive cell. The optical and elastic properties of the anti-perovskites are evaluated using the *thermo_pw*[47] package, while the thermal and thermoelectric properties are obtained with the *Gibbs2* code[48] and *BoltzTrap* code,[49] respectively. To assess thermal stability, *ab initio* molecular dynamics (AIMD) simulations are performed on $2 \times 1 \times 1$ supercells using the pw.x module of QE within the canonical (NVT) ensemble. The simulations employ the velocity Verlet integration scheme with the Andersen thermostat maintained at 300 K. A time step of 0.1 fs (femtosecond) is used over 10 000 steps, corresponding to a total simulation time of 10 ps (picosecond).

3 Results and discussion

3.1 Structural properties

3.1.1 Crystal structure. The pristine anti-perovskites A_3IO (A/A′ = K, Rb, Cs) adopt a cubic crystal structure belonging to the $Pm\bar{3}m$ space group (No. 221). Upon doping, the derivative compounds $A_{3-x}A'_xIO$ (A/A′ = K, Rb, Cs) transform into a tetragonal structure with $P4/mmm$ symmetry (No. 123). The unit cell geometries of all studied anti-perovskites are illustrated in Fig. 1. In these structures, the O atom occupies the Wyckoff position (0, 0, 0), while the I atom is located at (0.5, 0.5, 0.5). The alkali-metal cations (K, Rb, Cs) are positioned at (0.5, 0.5, 0), (0.5, 0, 0.5), and (0, 0.5, 0.5) Wyckoff positions. The unit cell configurations of the pristine compounds (K_3IO, Rb_3IO, and Cs_3IO), the 33.33% doped systems (K_2CsIO, K_2RbIO, Rb_2CsIO),

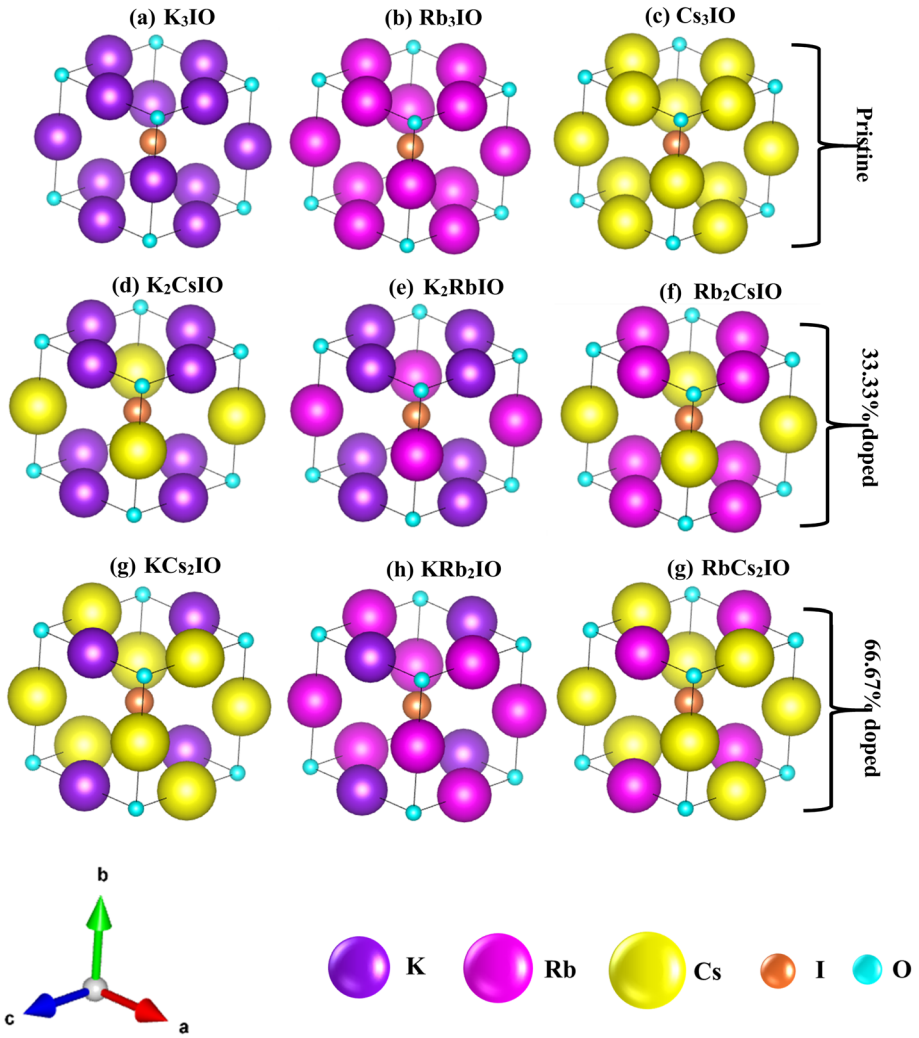

Fig. 1 Unit Cell of the pristine cubic structure (a–c) K_3IO, Rb_3IO, and Cs_3IO; 33.33% doped tetragonal structure (d–f) K_2CsIO, K_2RbIO, Rb_2CsIO; and 66.67% doped tetragonal structure (g–i) KCs_2IO, KRb_2IO, and $RbCs_2IO$, respectively. (b) Rb_3IO.

and the 66.67% doped systems (KCs_2IO, KRb_2IO, and $RbCs_2IO$) are identical to each other, except for the A-sites.

The variation of total energy with volume for the $A_{3-x}A'_xIO$ (A/A′ = K, Rb, Cs) anti-perovskites is presented in Fig. 2. The curves reveal a clear shift in the equilibrium volume as the cation at the A-site changes. This behaviour is expected and directly reflects the differences in the ionic radii of the constituent alkali metals. The optimised lattice parameters of the studied anti-perovskites are summarised in Table 1. A systematic increase in the lattice constants and volume is observed as the A-site is replaced by larger alkali metals, progressing from K → Rb → Cs. Another key parameter, formation energy, provides insight into the chemical stability of the compounds. The calculated formation energies are listed in Table 1. The negative formation energy values obtained for the $A_{3-x}A'_xIO$ (A/A′ = K, Rb, Cs) anti-perovskites indicate that these materials are chemically stable. Therefore, these compounds can be synthesizable under standard synthesis conditions. In addition, the goldsmith tolerance factor (GTF) has been calculated to assess the structural stability of the $A_{3-x}A'_xIO$ anti-perovskites, using the following equation:[50]

$$\mathrm{GTF} = \frac{r_I + r_A}{\sqrt{2}(r_O + r_A)} \quad (3)$$

Here, r_I, r_O, and r_A represent the effective ionic radii of the component I, O, and A (K, Rb, Cs), respectively. The GTF values for all studied anti-perovskites fall within the range of 0.892 to 0.911. This confirms the formation of stable three-dimensional perovskite structures, as the accepted stability range lies between 0.76 and 1.13.[51]

3.1.2 Lattice dynamic properties. To investigate the lattice dynamical behaviour of the studied compounds, phonon dispersion relations have been calculated at both 0 K and room temperature (300 K). Fig. 4 presents the harmonic phonon dispersion curves computed along the high-symmetry paths Γ-X-M-Γ-R for the cubic phases and Γ-X-M-Γ-Z for the tetragonal phases within the phonon Brillouin zone. Each primitive cell of the studied anti-perovskites consists of five atoms, resulting in a total of 15 vibrational modes.

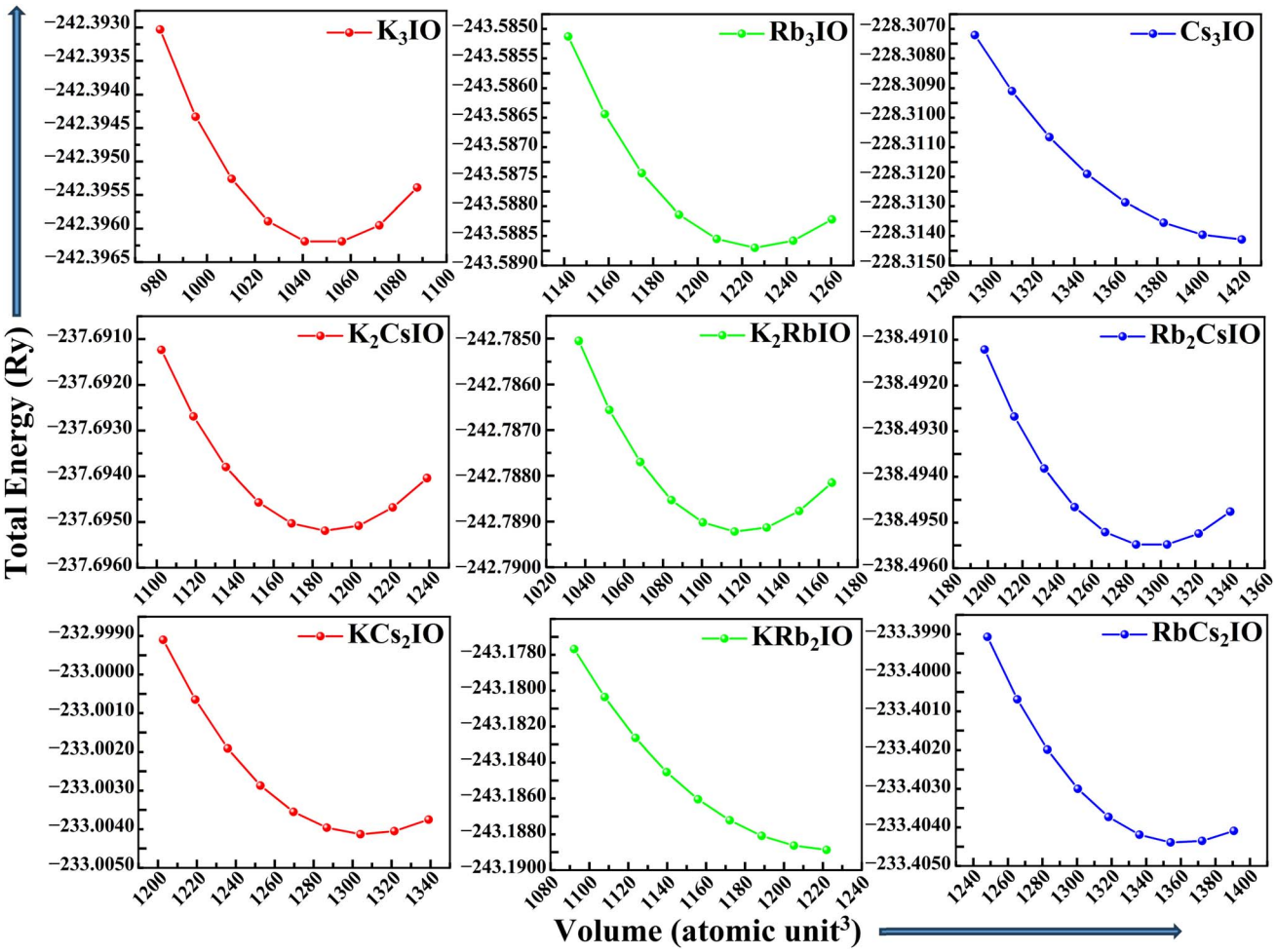

Fig. 2 Total energy as a function of the volume of the anti-perovskites $A_{3-x}A'_xIO$ (A/A′ = K, Rb, Cs).

Previous studies have shown that certain perovskite systems exhibit phonon instability at 0 K but become dynamically stable at elevated temperatures. For example, Ri *et al.* reported that $ACaH_3$ (A = Li, Na) perovskites are dynamically unstable at 0 K, whereas stability is recovered at 300 K.[55] Similarly, Tolborg *et al.* demonstrated the high-temperature stabilization of cubic zirconia arising from anharmonic lattice dynamics.[56] Similarly, the studied anti-perovskite compounds investigated in this work display phonon instability at 0 K. However, when lattice dynamics are evaluated at room temperature (300 K) using *ab initio* molecular dynamics, these previously unstable phases become dynamically stable. Furthermore, all nine studied anti-perovskites approach the classical Dulong–Petit limit at 300 K (Fig. 11), providing additional confirmation of their thermodynamic stability at room temperature.

Table 1 The optimised lattice parameters (*a*, *b*, *c*), volume (*V*), formation energy (ΔE_f), and Goldschmidt Tolerance Factor (GTF) of the A-site-doped anti-perovskites $A_{3-x}A'_xIO$ (A/A′ = K, Rb, Cs)

Compounds	*a* (Å)	*b* (Å)	*c* (Å)	*V* (Å^3)	ΔE_f (eV)	GTF
K_3IO (this work)	5.36	5.36	5.36	154.04	−2.51	0.911
K_3IO[52]	5.37	5.37	5.37	154.75	—	—
K_3IO[53]	5.38	5.38	5.38	155.72	—	—
Rb_3IO (this work)	5.64	5.64	5.64	179.00	−2.48	0.901
Rb_3IO[52]	5.66	5.66	5.66	181.61	—	—
Rb_3IO[53]	5.67	5.67	5.67	182.28	—	—
Cs_3IO (this work)	5.87	5.87	5.87	202.11	−2.42	0.892
Cs_3IO[54]	5.99	5.99	5.99	215.83	−2.99	1.081
K_2CsIO (this work)	5.85	5.44	5.44	173.04	−2.46	0.904
K_2RbIO (this work)	5.65	5.38	5.38	163.21	−1.86	0.907
Rb_2CsIO (this work)	5.32	5.67	5.67	170.82	−2.46	0.898
KCs_2IO (this work)	5.38	5.92	5.92	188.37	−2.44	0.897
KRb_2IO (this work)	5.38	5.66	5.66	172.05	−1.84	0.904
$RbCs_2IO$ (this work)	5.66	5.87	5.87	195.36	−2.44	0.895

For the pristine cubic compounds, the phonon spectra at 0 K display well-defined acoustic branches across the entire Brillouin zone. The absence of imaginary phonon modes in K_3IO and Rb_3IO confirms their dynamical stability in the cubic phase. In contrast, Cs_3IO exhibits approximately 12.5% soft phonon modes near the zone centre and along selected high-symmetry directions, indicating lattice instability. This behaviour can be attributed to the larger ionic radius of Cs^+, which weakens the interatomic restoring forces and results in a comparatively softer lattice. However, at 300 K, Cs_3IO exhibit stabilization of the low-frequency vibrational modes. The acoustic branches remain positive throughout the Brillouin zone. This stabilization is associated with stronger anharmonic

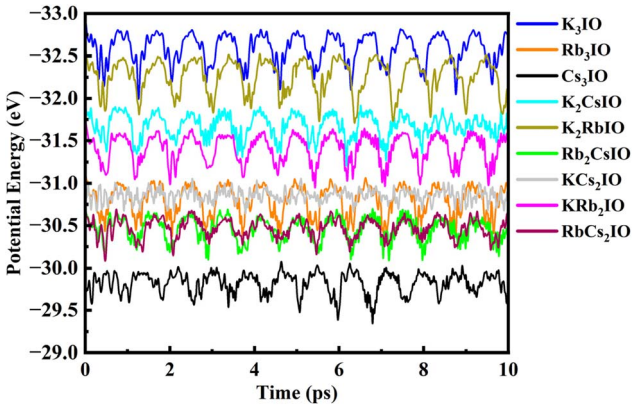

Fig. 3 Calculated thermal stability through AIMD of the $A_{3-x}A'_xIO$ (A/A′ = K, Rb, Cs) anti-perovskites at 300 K.

lattice vibrations at room temperature, which remove the low-energy instabilities present at 0 K. The stablization can be validated through the experimental synthesis of Cs_3IO by Feldmann *et al.*[31]

For the 33.33% doped structures (K_2CsIO, K_2RbIO, and Rb_2CsIO) and 66.67% doped structures (KCs_2IO, KRb_2IO, and $RbCs_2IO$), the phonon dispersions show a noticeable redistribution of vibrational modes due to their reduced crystal symmetry. In K_2RbIO, approximately 5% weak imaginary frequencies are present at 0 K but disappear at 300 K, suggesting that thermal effects dynamically stabilize the tetragonal structure. Similarly, $RbCs_2IO$ exhibits approximately 22.5% low-frequency instabilities at 0 K, especially near the Brillouin zone boundaries. This reflects increased lattice anharmonicity and local structural distortions induced by higher alkali-site doping. Upon increasing the temperature to 300 K, the phonon spectra become entirely positive. It confirms the thermodynamic stability of these phases at 300 K. Moreover, the AIMD outputs (Fig. 3) show stable potential energy profiles with only minor fluctuations within a narrow range, indicating the absence of structural degradation or phase transitions during the simulation. These limited energy variations confirm the thermal stability of the systems and demonstrate that their structural integrity is preserved at room temperature.

The high-frequency phonon modes are particularly important in polar semiconductors, where they show long-range phonon-electron interactions through the Fröhlich mechanism.[57] This influences the lattice thermal conductivity and carrier scattering processes. Such interactions have direct implications for thermoelectric efficiency. Overall, the phonon dispersion and AIMD analysis confirm the dynamical and thermal feasibility of the studied compounds and provide a basis for understanding their thermal transport behaviour and suitability for thermoelectric applications.

3.2 Electronic properties

Electronic properties define how a material behaves under electromagnetic fields, determined by electron configuration, energy bands, and density of states (DOS). This section discusses the calculated electronic band structures, density of states, and charge density distributions of the $A_{3-x}A'_xIO$ (A/A′ = K, Rb, Cs) anti-perovskites.

3.2.1 Band structure analysis. The electronic band structures are evaluated using the PBE, RPBE, and HSE06 exchange-correlation functionals, as shown in Fig. 5 and summarised in Table 2. Both the GGA-PBE and GGA-RPBE show an underestimated band gap, whereas HSE06 calculates the band gap close to the experimental value. For example, Das *et al.* studied 36 synthesized halide perovskites, which show that the HSE06 hybrid functional significantly improves band gap prediction. The ratio of the experimental bandgap and the HSE06 band gap of some perovskites is as follows:[58] 1.67/1.61 ($CsGeI_3$), 1.23/1.15 ($CsSnI_3$), 1.28/1.31 ($MASnI_3$), 1.4/1.5 ($FASnI_3$) and so on. Though RPBE underestimate the band gap but improves the value over the PBE.

The pristine compounds K_3IO, Rb_3IO, and Cs_3IO exhibit a monotonic decrease in the band gap (HSE06), from 2.19 eV for K_3IO to 1.63 eV for Rb_3IO and 1.56 eV for Cs_3IO. This behaviour arises from the increasing ionic radius and polarizability of the A-site cations. As a consequence, it leads to lattice expansion and reduces the bonding-antibonding splitting between the I-5p and O-2p states that define the band edges,[59,60] as shown in Fig. 7. As a result, the conduction band minimum shifts toward lower energies, producing a narrower band gap as K is progressively replaced by Rb and Cs.

Partial substitution at the A-site with a second alkali metal at a concentration of 33.33% reduces the crystal symmetry from cubic to tetragonal and results in a further narrowing of the band gap. The HSE06 band gaps for the K_2CsIO, K_2RbIO, and Rb_2CsIO are respectively 1.61 eV, 1.67 eV and 1.41 eV. The presence of two different alkali cations with different ionic radii introduces local lattice distortions and creates a nonuniform electrostatic environment around the IO_3 units,[61] as shown in Fig. 8. These effects increase band-edge dispersion and induce bandgap bowing[62] compared to the corresponding cubic parent compounds. In IIIA-VA semiconductors, it is common that alloys such as InGaN (indium gallium nitride)[63] and AlGaAs (aluminium gallium arsenide)[64] exhibit significant bandgap bowing. Band gap bowing refers to the non-linear, downward bowing behaviour of the electronic band gap in semiconductor alloys as a function of composition. It is primarily driven by structural relaxation, local atomic size differences, and electronegativity differences.[62] Following this, the 66.67% doped tetragonal phases also exhibit a reduced band gap bowing than their corresponding pristine compounds. The HSE06 band gaps of KCs_2IO, KRb_2IO, and $RbCs_2IO$ are respectively 1.61 eV, 1.54 eV and 1.47 eV. Notably, the ionic size mismatch between Rb^+ and Cs^+ strongly enhances bandgap bowing in Rb_2CsIO (1.41 eV) and $RbCs_2IO$ (1.47 eV), leading to even a smaller bandgap than the pristine Cs_3IO (1.56 eV) compound.

All the studied compounds exhibit a direct band gap at the gamma (Γ) symmetry point, which is a critical prerequisite for efficient optoelectronic and photovoltaic applications. Direct band gap materials enable strong optical absorption without phonon assistance. It leads to reduced absorber thickness and improved carrier collection efficiency. This characteristic, combined with the tunability of the band gap through alkali-

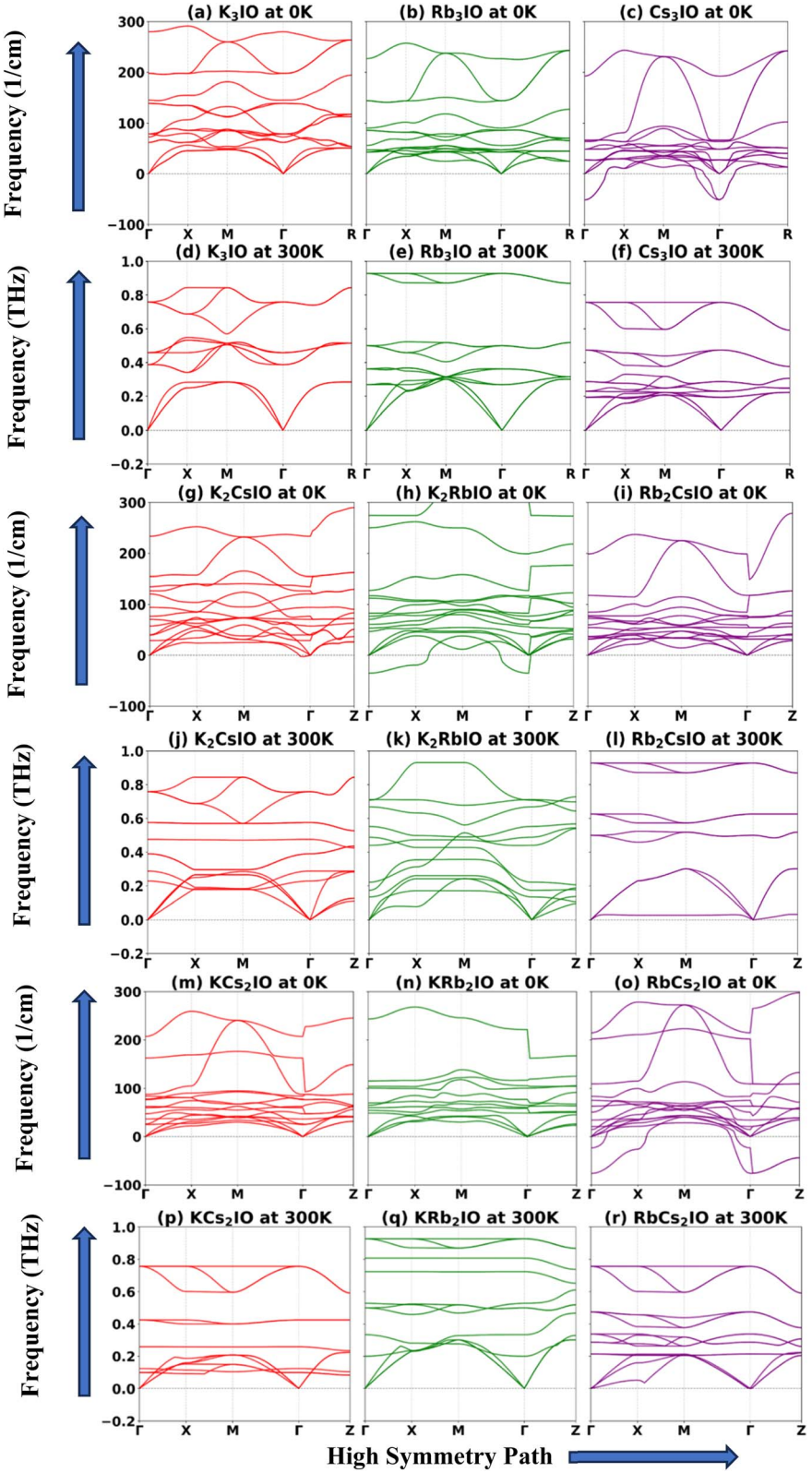

Fig. 4 Phonon dispersion curves of the pristine cubic structure (a–c) & (d–f) K_3IO, Rb_3IO, and Cs_3IO; 33.33% doped tetragonal structure (g–i) & (j–l) K_2CsIO, K_2RbIO, Rb_2CsIO; and 66.67% doped tetragonal structure (m–o) & (p–r) KCs_2IO, KRb_2IO, and $RbCs_2IO$, at 0 K and 300 K, respectively.

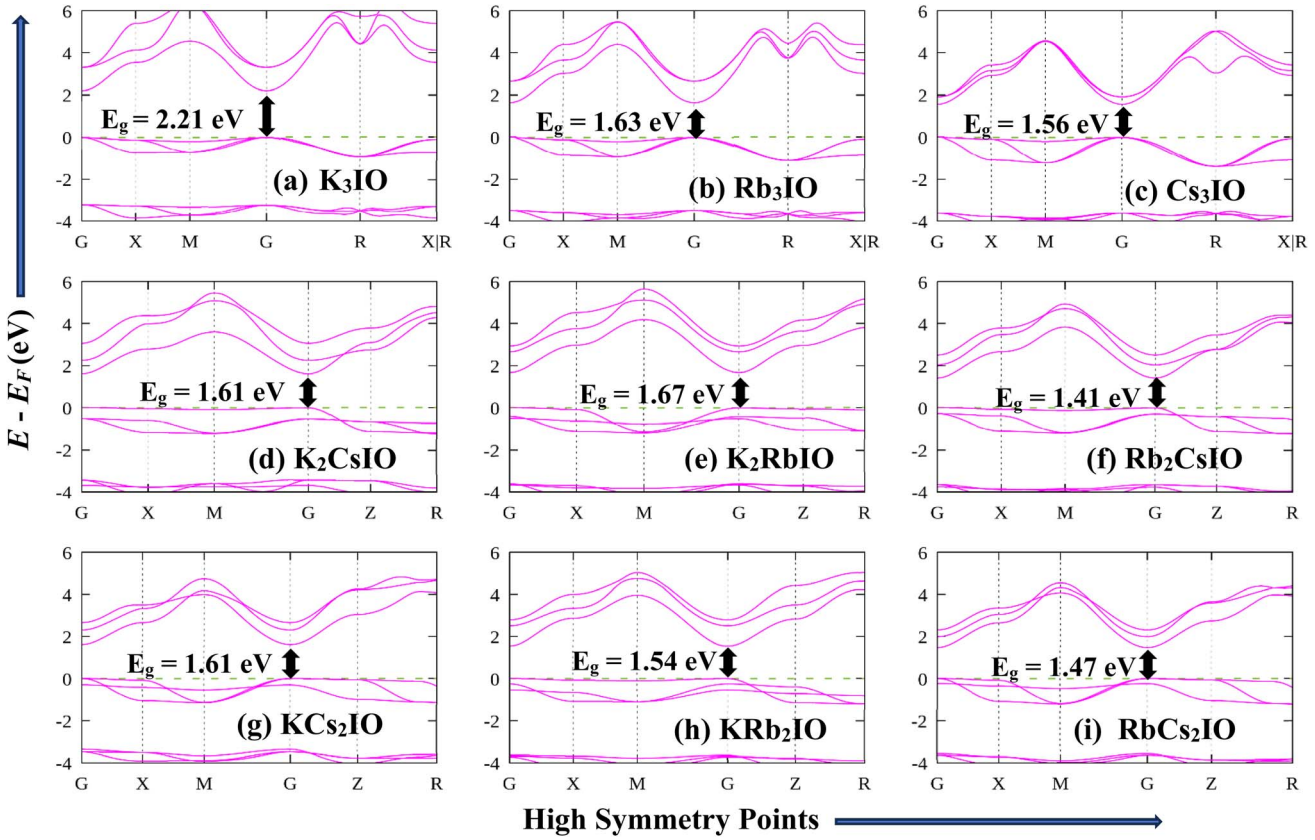

Fig. 5 Energy band diagrams of the pristine cubic structures (a–c) K_3IO, Rb_3IO, and Cs_3IO; 33.33% doped tetragonal structures (d–f) K_2CsIO, K_2RbIO, Rb_2CsIO; and 66.67% doped tetragonal structures (g–i) KCs_2IO, KRb_2IO, and $RbCs_2IO$, respectively.

metal doping, results in potential photovoltaic applications. Such as photodetectors, light-emitting devices, and optoelectronic sensors operating across the visible to near-infrared range. Notably, A-site doping shifts the band gaps toward the optimal range (1.34 eV)[65] predicted by the Shockley–Queisser limit for single-junction solar cells. Fig. 6(a) illustrates the Shockley–Queisser limit efficiency,[66] showing the maximum photovoltaic efficiency for an array of band gaps ranging from 0.5 to 3.0 eV. The studied anti-perovskites fall within the region of 1.41 to 2.21 eV, which leads to enhanced PCE as shown in Fig. 6(b). Overall, A-site doping effectively tunes the E_g, resulting in better PCE than their corresponding pristine compounds.

Table 2 Calculated band gaps of the anti-perovskites $A_{3-x}A'_xIO$ (A/A′ = K, Rb, Cs) using GGA-PBE, GGA-RPBE, and HSE06 approximation

	Band gap (eV)		
Compounds	GGA-PBE	GGA-RPBE	HSE06
K_3IO (this work)	1.05	1.23	2.21
K_3IO[52]	1.02	—	2.19
K_3IO[53]	—	—	2.18
Rb_3IO (this work)	0.55	0.74	1.63
Rb_3IO[52]	0.53	—	1.69
Rb_3IO[53]	—	—	1.61
Cs_3IO (this work)	0.51	0.73	1.56
Cs_3IO[54]	0.21	—	1.52
K_2CsIO (this work)	0.50	0.68	1.61
K_2RbIO (this work)	0.56	0.74	1.67
Rb_2CsIO (this work)	0.33	0.53	1.41
KCs_2IO (this work)	0.50	0.69	1.61
KRb_2IO (this work)	0.43	0.61	1.54
$RbCs_2IO$ (this work)	0.61	0.62	1.47

Moreover, the flat energy bands in the valence band maxima (Fig. 5) may generated due to the large differences in the electronegativities between the elements O and host alkali metals/heavily doping alkali metal atoms (K, Rb and Cs).[67] This flatness indicates energy changes very little with momentum, allowing many electronic states to exist within a narrow energy range. This high concentration of states allows for many charge carriers to contribute to transport.[68] As a result, it induces high electrical conductivity, high Seebeck coefficient, and correspondingly excellent values of PF and ZT.[69] Following this, the studied compounds have shown good thermoelectric behaviour, which has been described in the Section 3.6.

3.2.2 Density of states analysis (DOS). The total and partial density of states (TDOS and PDOS) are calculated to clarify the orbital contributions near the band edges. They also help to explain the bandgap modulation across the cubic and tetragonal phases of the $A_{3-x}A'_xIO$-based compounds, as shown in Fig. 7. For all cubic compounds, the TDOS exhibits a clear semiconducting character with a finite band gap at the Fermi level. The PDOS analysis indicates that the valence band maximum (VBM) is primarily composed of O-2p states, with a notable contribution from I-5p orbitals. It reflects strong p–p

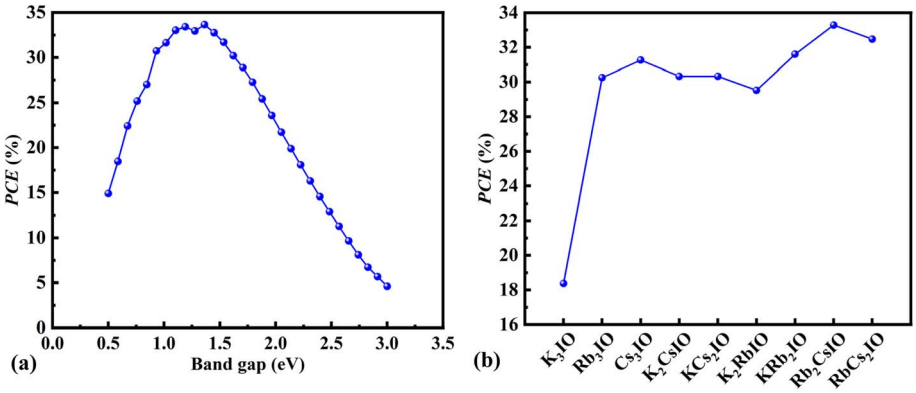

Fig. 6 (a) Calculated Shockley Queisser efficiency limit for an array of band gaps, (b) estimated photovoltaic efficiency for the studied compounds at 300 K temperature under AM1.5G solar spectrum.

hybridisation within the IO_3 framework.[70] In contrast, the conduction band minimum (CBM) primarily originates from the s-orbitals of the alkali metals (K-s, Rb-s, or Cs-s). As the A-site cation changes from K → Rb → Cs, the s-state of these alkali-metal ions moves closer to the Fermi level. As a result, a systematic downward shift of the CBM has been observed. This behaviour accounts for the progressive reduction of the band gap from K_3IO to Cs_3IO.

In the 33.33% doped compounds (K_2CsIO, K_2RbIO, and Rb_2CsIO) and the 66.67% doped phases (KCs_2IO, KRb_2IO, $RbCs_2IO$), the TDOS confirms the retention of semiconducting behaviour, although the band gaps are reduced relative to the cubic phases, as mentioned earlier. In the valence band, increased hybridization occurs between O-2p and I-5p states induced by symmetry lowering and local lattice distortions. The presence of two different alkali cations leads to partial splitting and redistribution of alkali-metal s-states in the conduction band.[71] Overall, the heavier alkali species (Rb or Cs) strongly drive the s-orbitals (near the CBM) toward lower energies. On the contrary, enhanced hybridization between O-2p and I-5p states disperses the valence-band edge. As a result, the coexistence of two different-sized cations leads to non-linear band-edge shifting and pronounced bandgap bowing.

3.2.3 Charge density analysis. The contour plots shown in Fig. 8 depict the electronic charge density and provide insight into the nature of chemical bonding in the anti-perovskite compounds. The high concentration of contour lines around the atomic centres indicates strong charge localisation, which is characteristic of predominantly ionic bonding. The iodine atom at the body centre and the oxygen atoms at the corners display nearly spherical charge distributions. The absence of charge sharing or continuous charge bridges between the I/O anions and the alkali-metal cations suggests that the valence electrons are largely transferred to the more electronegative species. Therefore, it confirms the ionic nature of the $A_{3-x}A'_xIO$ lattice structures. As the size of the alkali-metal cation increases from K^+ to Cs^+, the interatomic regions expand noticeably. This trend is consistent with the increase in lattice parameters and the lower electronegativity of the heavier alkali metals, both of which favour enhanced charge separation within the lattice.

Comparing the pristine cubic structure with the doped tetragonal phases highlights the effect of cation substitution on the local electronic environment. The electron density maps clearly distinguish two different cation species. The (100/010/001) plane of pristine cubic structures, the (001) plane of 33.33% doped tetragonal structures and the[100] plane of 66.67% doped tetragonal structures show uniform charge density around the central iodine atom due to the presence of the same alkali cation species. On the contrary, the differences in ionic radii (due to the different cation species) in the (100/010) plane of 33.33% doped structures and the (010/001) plane of 66.67% doped structures introduce local lattice distortions, which result in non-uniform charge density contours around the central iodine atom. In the doped structures, the electronic environment is largely governed by the secondary cation, resulting in diverse mechanical, optical, and thermoelectric properties, as described later. Despite this change, the charge density remains strongly localized, indicating ionic and semiconducting character of the mixed-cation systems. The electron density maps further support the presence of strong coulombic interactions in these anti-perovskites.

3.3 Mechanical properties

Elastic properties describe a material's response to an applied load and its recovery to its original shape when the load is removed. Mechanical stability can be ensured through the elastic constants, which provide insight into the nature of the crystal framework's bonding. Following this, key mechanical behaviours such as Young's modulus (Y), bulk (B), and shear moduli (G), elastic anisotropy (A^U), Poisson's ratio (ν), and the tendency toward brittle or ductile behaviour has been assessed in this section.

Using the "stress–strain" principle, the elastic constants of $A_{3-x}A'_xIO$ (A/A′ = K, Rb, and Cs) anti-perovskites are calculated, which are listed in Table 3. The Born stability criteria are utilized to evaluate mechanical stability. For cubic and tetragonal structures, the conditions are given below, respectively:[72]

For cubic structures:

$$C_{11} + 2C_{12} > 0,\ C_{11} - C_{12} > 0\ \&\ C_{11},\ C_{44} > 0 \quad (4)$$

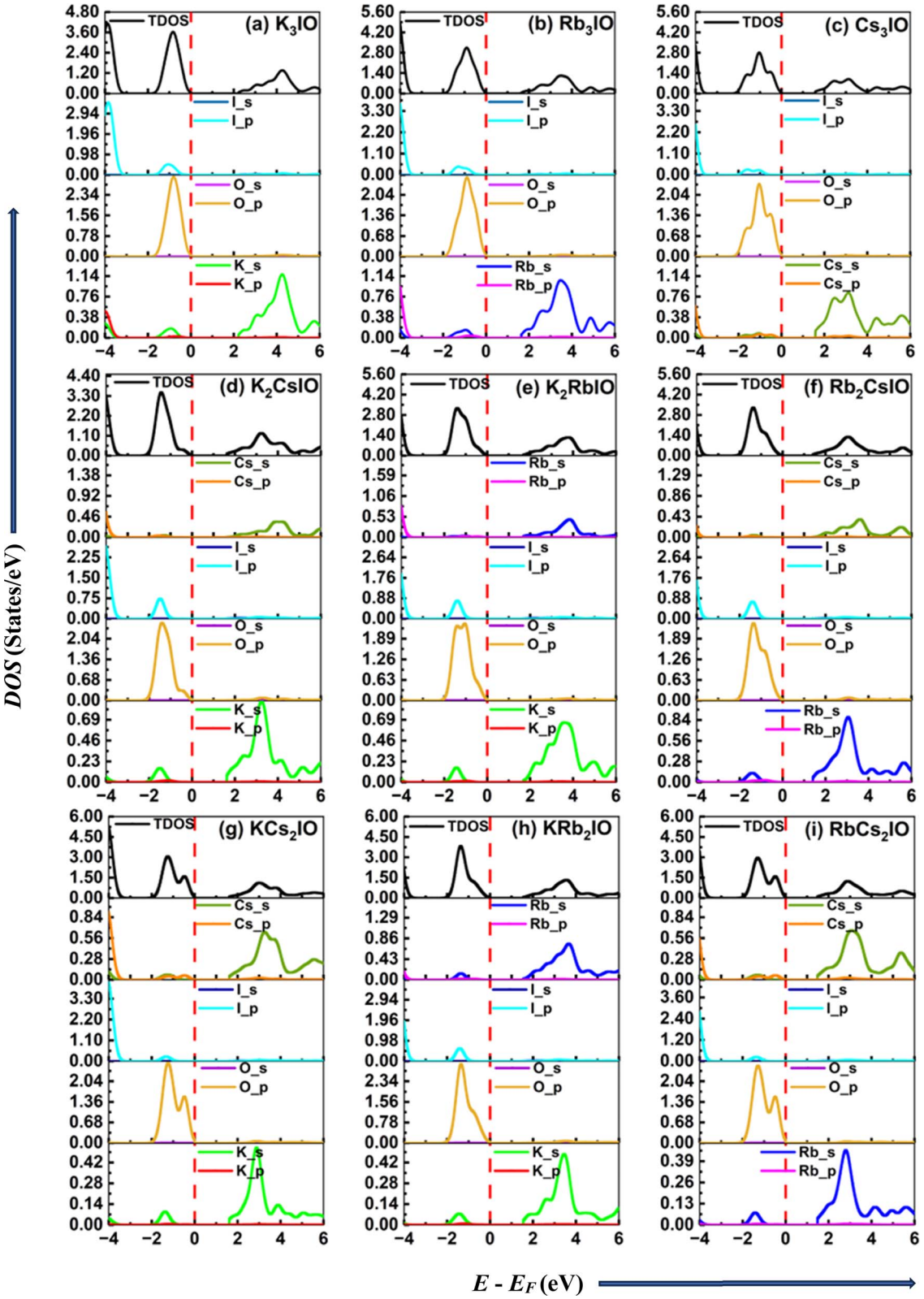

Fig. 7 Total and partial density of states of the pristine cubic structure K_3IO, Rb_3IO, and Cs_3IO; 33.33% doped tetragonal structure K_2CsIO, K_2RbIO, Rb_2CsIO; and 66.67% doped tetragonal structure KCs_2IO, KRb_2IO, and $RbCs_2IO$, respectively.

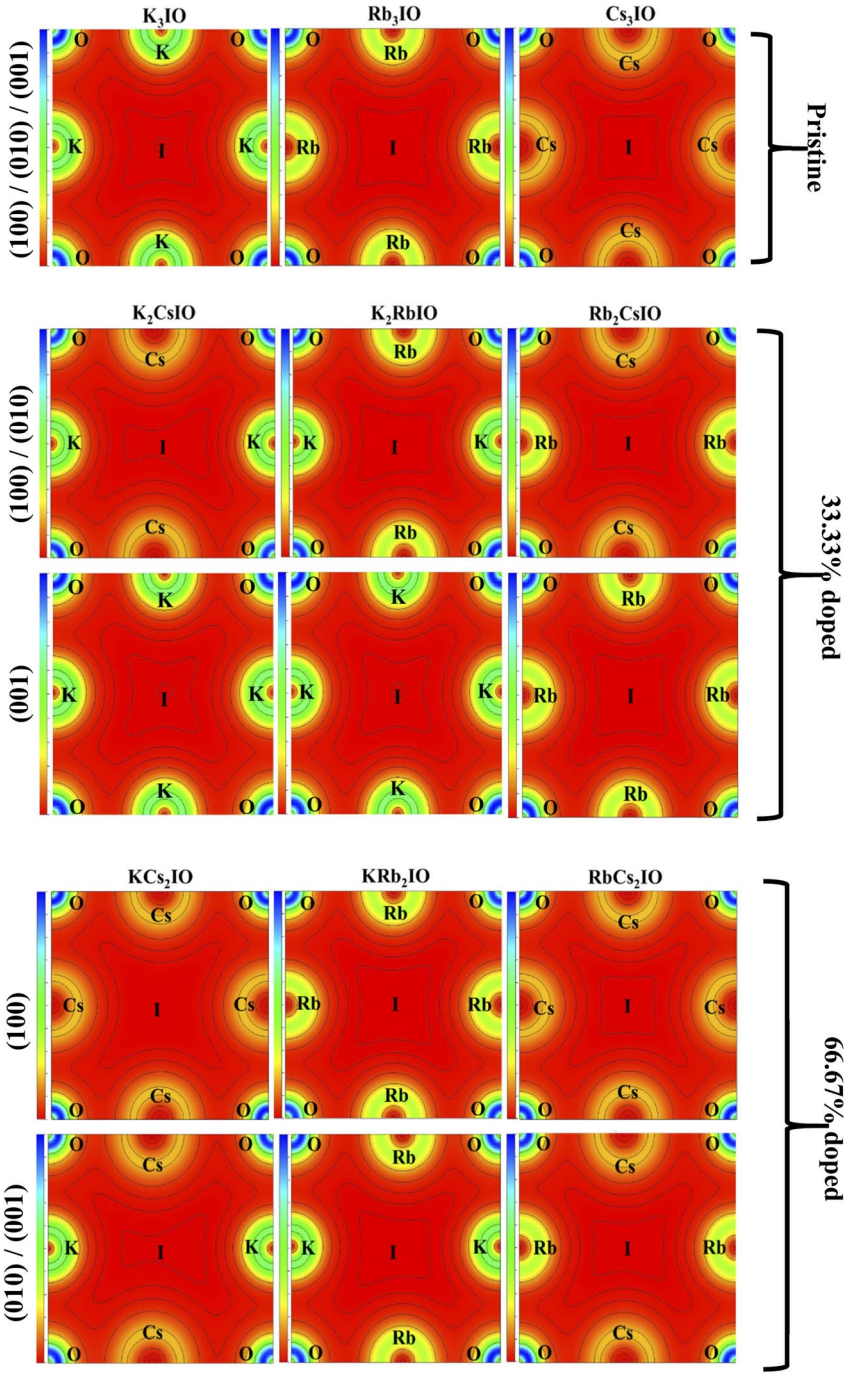

Fig. 8 Electron density of the pristine cubic structure K_3IO, Rb_3IO, and Cs_3IO at (100/010/001) plane; 33.33% doped tetragonal structure K_2CsIO, K_2RbIO, Rb_2CsIO at (100/010) & (001) planes; and 66.67% doped tetragonal structure KCs_2IO, KRb_2IO, and $RbCs_2IO$ at[100] & (010/001) planes, respectively.

For tetragonal structures:

$$C_{11} + C_{33} - 2C_{13} > 0,\ C_{11} - C_{12} > 0,\ 2C_{11} + C_{33} + 2C_{12} + 4C_{13} > 0\ \&\ C_{11},\ C_{33},\ C_{44},\ C_{66} > 0 \quad (5)$$

All the anti-perovskites have fulfilled the mechanical stability conditions, which have been confirmed by their calculated elastic constants, tabulated in Table 3. Therefore, the compounds are mechanically stable. Additionally, a higher value of the elastic constant C_{11} indicates greater incompressibility along the x-direction.[73] The C_{44} is widely regarded as a reliable indicator of resistance to shear deformation and, consequently, of solid hardness.[74] Among all the studied anti-perovskites, K_2RbIO exhibits the highest compressibility and the greatest resistance to deformation, as reflected by its elastic constant values (Table 3).

For cubic structures, the bulk (B_V, B_R) and shear modulus (G_V, G_R) have been calculated using the following equations:[75]

Table 3 Calculated elastic constants of the pristine cubic structure K_3IO, Rb_3IO, and Cs_3IO; 33.33% doped tetragonal structure K_2CsIO, K_2RbIO, Rb_2CsIO; and 66.67% doped tetragonal structure KCs_2IO, KRb_2IO, and $RbCs_2IO$, respectively

Compounds	C_{11}	C_{12}	C_{13}	C_{33}	C_{44}	C_{66}
K_3IO (this work)	37.18	9.23	—	—	11.96	—
K_3IO[52]	35.50	7.44	—	—	12.00	—
K_3IO[53]	42.15	9.35	—	—	12.23	—
Rb_3IO (this work)	31.80	7.83	—	—	9.32	—
Rb_3IO[52]	31.82	7.88	—	—	9.31	—
Rb_3IO[53]	35.91	7.78	—	—	9.55	—
Cs_3IO (this work)	26.25	7.72	—	—	7.43	—
Cs_3IO[54]	30.84	9.50	—	—	6.92	—
K_2CsIO (this work)	30.72	13.06	6.15	31.58	7.75	15.61
K_2RbIO (this work)	48.89	9.34	9.69	21.68	12.42	9.76
Rb_2CsIO (this work)	29.67	9.94	6.83	29.80	7.64	10.80
KCs_2IO (this work)	28.50	6.31	9.50	29.04	10.18	5.99
KRb_2IO (this work)	28.86	8.53	7.66	28.46	7.71	10.40
$RbCs_2IO$ (this work)	27.55	6.34	8.28	27.45	8.84	6.50

$$B_V = B_R = \frac{(C_{11} + 2C_{12})}{3} \quad (6)$$

$$G_V = \frac{C_{11} - C_{12} + 3C_{44}}{5} \quad (7)$$

$$G_R = \frac{5(C_{11} - 5C_{12})C_{44}}{3(C_{11} - 5C_{12}) + 4C_{44}} \quad (8)$$

Similarly, for tetragonal structures, the bulk (B_V, B_R) and shear modulus (G_V, G_R) have been calculated using the following equations:[75](Subscript letter V and R denote Voigt and Reuss approximation, respectively).

$$B_V = \frac{[2(C_{11} + C_{12}) + C_{33} + 4C_{13}]}{9} \quad (9)$$

$$B_R = \frac{C_{33}(C_{11} + C_{12}) - 2C_{13}^2}{C_{11} + C_{12} + 2C_{33} - 4C_{13}} \quad (10)$$

$$G_V = \frac{4C_{11} - 2C_{12} + 2C_{33} - 4C_{13} + 12C_{44} + 6C_{66}}{30} \quad (11)$$

$$G_R = 15\left[\frac{2(2C_{11} + 2C_{12} + 42C_{13} + C_{33})}{C_{33}(C_{11} + C_{12}) - 2C_{13}^2} + \frac{6(C_{11} - C_{12} + C_{44})}{C_{44}(C_{11} - C_{12})} + \frac{3}{C_{66}}\right]^{-1} \quad (12)$$

Using the Voigt and Reuss approximation value, the Hill approximation bulk (B_H) and shear modulus (G_H) have been calculated using the following equations:[75]

$$B_H = \frac{B_V + B_R}{2} \quad (13)$$

$$G_H = \frac{G_V + G_R}{2} \quad (14)$$

Considering the Voigt–Reuss–Hill approximation, the Poisson's ratio (υ), young modulus (Y), and universal anisotropy index (A^U) have been measured by the following equations:[75]

$$\upsilon = \frac{3B_H - 2G_H}{2(3B_H + G_H)} \quad (15)$$

$$Y = \frac{9B_H G_H}{(3B_H + G_H)} \quad (16)$$

$$A^U = 5\frac{G_V}{G_R} + \frac{B_V}{B_R} - 6 \geq 0 \quad (17)$$

The modulus Y, B and G depend strongly on the atomic arrangement and charge density within the crystal lattice and the strength of the interatomic interactions. In general, these moduli decrease as the interatomic distance increases, since the corresponding interatomic forces become weaker.[73] A similar trend is observed in the present compounds, tabulated in Table 4, where these moduli have systematically decreased as

Table 4 Calculated bulk modulus (Voigt B_V, Reuss B_R and Hill B_H), shear modulus (Voight G_V, Reuss G_R and Hill G_H), young modulus (Y), Poisson's ratio (υ), Pugh's ratio (B/G), machinability index (B/C_{44}) and universal anisotropy index (A^U) of the pristine cubic structure K_3IO, Rb_3IO, and Cs_3IO; 33.33% doped tetragonal structure K_2CsIO, K_2RbIO, Rb_2CsIO; and 66.67% doped tetragonal structure KCs_2IO, KRb_2IO, and $RbCs_2IO$, respectively

Compounds	B_V	G_V	B_R	G_R	B_H	G_H	Y	υ	B/G	B/C_{44}	A^U
K_3IO (this work)	18.55	12.77	18.55	12.69	18.55	12.73	31.08	0.22	1.46	1.55	0.03
K_3IO[52]	—	—	—	—	16.80	12.82	—	—	1.31	—	—
K_3IO[53]	—	—	—	—	20.28	—	33.66	—	1.31	—	—
Rb_3IO (this work)	15.83	10.38	15.82	10.23	15.82	10.38	25.56	0.23	1.52	1.70	0.07
Rb_3IO[52]	—	—	—	—	15.86	10.57	—	—	1.50	—	—
Rb_3IO[53]	—	—	—	—	17.15	11.15	27.51	—	1.50	—	—
Cs_3IO (this work)	13.89	8.16	13.89	8.07	13.89	8.12	20.38	0.26	1.71	1.87	0.06
Cs_3IO[54]	—	—	—	—	16.61	8.23	21.21	0.28	2.01	2.40	—
K_2CsIO (this work)	15.97	10.73	15.88	9.83	15.92	10.28	25.37	0.23	1.55	2.05	0.46
K_2RbIO (this work)	17.83	11.37	16.85	10.66	17.35	11.02	27.28	0.24	1.57	1.40	0.39
Rb_2CsIO (this work)	15.15	9.59	15.01	9.26	15.08	9.42	23.40	0.24	1.60	1.97	0.18
KCs_2IO (this work)	15.18	9.32	15.32	8.9	15.25	9.10	22.78	0.25	1.67	1.50	0.22
KRb_2IO (this work)	16.34	10.65	15.77	10.14	16.06	10.39	25.66	0.23	1.55	2.08	0.29
$RbCs_2IO$ (this work)	14.24	8.8	14.35	8.59	14.29	8.69	21.68	0.25	1.64	1.62	0.11

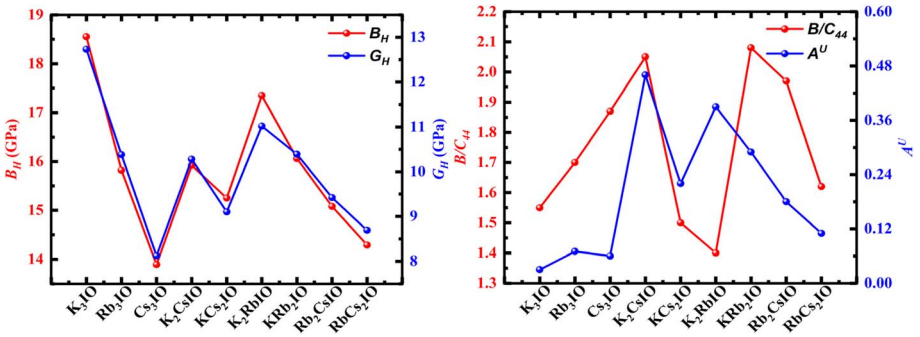

Fig. 9 Calculated Bulk (B_H) and Shear moduli (G_H), machinability index (B/C_{44}) and universal anisotropy index (A^U) trend of the $A_{3-x}A'_xIO$ (A/A′ = K, Rb, and Cs) anti-perovskites.

the A-site cation changes from K → Rb → Cs in the cubic phases. As the A-site cation size increases from K to Cs, the charge density becomes more diffuse due to the reduced electronegativity and larger ionic radius of the heavier alkali metals. This redistribution weakens the electrostatic interaction between the cations and the IO framework, leading to a gradual reduction in elastic moduli. In the tetragonal doped structures, the 66.67% doped compositions exhibit lower moduli values than their corresponding 33.33% doped counterparts, reflecting the enhanced lattice expansion and reduced interatomic interactions at higher dopant concentrations. The non-uniform charge density fluctuations weaken specific bonding directions, reducing shear and bulk moduli. Therefore, the 33.33% doped structures exhibit greater resistance to applied pressure and higher stiffness than the 66.67% doped counterparts.

The Pugh ratio (B/G) is commonly used to distinguish between brittle and ductile behaviour in solids. Ductile materials show $B/G > 1.75$, whereas compounds lower than this threshold value are considered brittle.[76] Poisson's ratio (υ) provides an additional criterion for mechanical classification. According to Frantsevich's rule, materials with $\upsilon > 0.26$ exhibits ductile behaviour, while lower values indicate brittleness.[77] As shown in Table 4, all studied phases fall within the brittle regime. However, the 66.67% doped compounds display reduced brittleness compared with their 33.33% doped counterparts, while the pristine cubic compounds show a gradual tendency toward ductility as the A-site cation size increased from K → Rb → Cs. These phenomena can be explained by the partial delocalization of charge density through lattice expansion and doping, which promotes increased ductility. The presence of weaker, more ionic A–O interactions facilitates plastic deformation through easier bond rotation under applied stress.

The B/C_{44} ratio describes the machinability of any material being processed.[78] Materials with lower C_{44} values and reduced resistance to shear deformation generally exhibit better machinability, as shown in Fig. 9. An overall increase in machinability is observed as the A-site cation size increases from K → Rb → Cs. The 33.33% doped structures show higher B/C_{44} ratios than their corresponding 66.67% doped phases, except K_2RbIO and KRb_2IO. This is because K_2RbIO shows the highest resistance to deformation, as mentioned earlier.

The universal anisotropy index ($A\square$) provides a measure of elastic isotropy. A fully isotropic material shows $A^U = 0$.[79] Deviations from zero correspond to the degree of anisotropy. As shown in Table 4 and Fig. 9, K_2CsIO (0.46) has the largest deviation among the studied compounds, suggesting it is the most anisotropic. Though the value is not too large to be an extensive anisotropic material. Overall, the 33.33% doped structures show higher elastic anisotropy than their corresponding 66.67% doped counterparts, while the pristine cubic phases remain nearly isotropic.

The mechanical properties are closely related to thermoelectric performance through their influence on lattice dynamics and phonon transport. Compounds with lower elastic moduli (bulk and shear) and higher ductility typically exhibit softer lattices, which enhance phonon–phonon scattering and reduce lattice thermal conductivity (K_L).[80] This reduction in K_L is beneficial for improving the thermoelectric figure of merit (ZT). Additionally, high-strength structures ensure structural integrity at elevated temperatures, which is essential for reliable thermoelectric operation. Therefore, there should be a balance between ductility and strength to perform the material properly and effectively in the thermoelectric condition.

3.4 Thermal properties

In this work, the relevant thermodynamic parameters are evaluated over a temperature range of 0–800 K. Within this range, the quasi-harmonic Debye model is applicable and provides reliable estimates of temperature-dependent material properties.[81] The Debye temperature (θ_D) is a key thermodynamic parameter, as it is closely related to several fundamental physical properties, including melting temperature, heat capacity, and elastic stiffness.[81] When the temperature significantly exceeds θ_D, all lattice vibrational modes are thermally activated and obey the classical limit.[82] In contrast, when the temperature falls well below θ_D, high-frequency vibrational modes become frozen, and lattice dynamics are dominated primarily by low-frequency acoustic phonons.[82] Physically, θ_D represents the characteristic temperature corresponding to the maximum phonon frequency that can be excited within a crystal lattice. In the present study, the Debye temperature is estimated using the following expression:[83]

Table 5 Calculated crystal density (ρ), debye temperature (θ_D), longitudinal (ϑ_l), transverse (ϑ_t), average sound velocity (ϑ_m), and melting temperature (T_m) of the pristine cubic structure K_3IO, Rb_3IO, and Cs_3IO; 33.33% doped tetragonal structure K_2CsIO, K_2RbIO, Rb_2CsIO; and 66.67% doped tetragonal structure KCs_2IO, KRb_2IO, and $RbCs_2IO$, respectively

Compounds	ρ (kg m^{-3})	θ_D (K)	ϑ_l (ms^{-1})	ϑ_t (ms^{-1})	ϑ_m (ms^{-1})	T_m (K)
K_3IO (this work)	2779	224	3574	2140	2366	772
K_3IO[53]	—	233	—	—	—	—
Rb_3IO (this work)	3702	167	2846	1680	1859	740
Rb_3IO[53]	—	174	—	—	—	—
Cs_3IO (this work)	4447	131	2407	1379	1531	708
Cs_3IO[54]	4160	—	—	—	—	735
K_2CsIO (this work)	3392	175	2978	1754	1925	493
KCs_2IO (this work)	3952	150	2671	1540	1702	483
K_2RbIO (this work)	3121	192	3231	1894	2072	533
KRb_2IO (this work)	3421	102	3048	1797	1136	483
Rb_2CsIO (this work)	3948	152	2674	1561	1726	487
$RbCs_2IO$ (this work)	4201	140	2521	1461	1617	477

$$\theta_D = \frac{h}{k_B}\left[\left(\frac{3n}{4\pi}\right)N_A\rho/M\right]\vartheta_m \quad (18)$$

Here, h, n, k_B, r, N_A, and M represent Planck's constant, the number of atoms in the molecule, Boltzmann's constant, mass density, Avogadro's number, and molar mass, respectively. The average elastic velocity (ϑ_m), which is connected to the θ_D have been calculated using:[83]

$$\vartheta_m = \left[\frac{1}{3}\left(\frac{1}{\vartheta_l^3} + \frac{2}{\vartheta_t^3}\right)\right]^{-\frac{1}{3}} \quad (19)$$

In crystalline solids, the longitudinal (ϑ_l) and transverse (ϑ_t) sound velocities are governed by the elastic properties and mass density of the material and are directly related to the bulk modulus and shear modulus through Navier's equations,[83] which are given below:

$$\vartheta_l = [(3B + 4G)/3\rho]^{1/2} \quad (20)$$

$$\vartheta_t = [G/\rho]^{1/2} \quad (21)$$

In general, the longitudinal sound velocity is significantly higher than the transverse velocity.[84] Since transverse waves

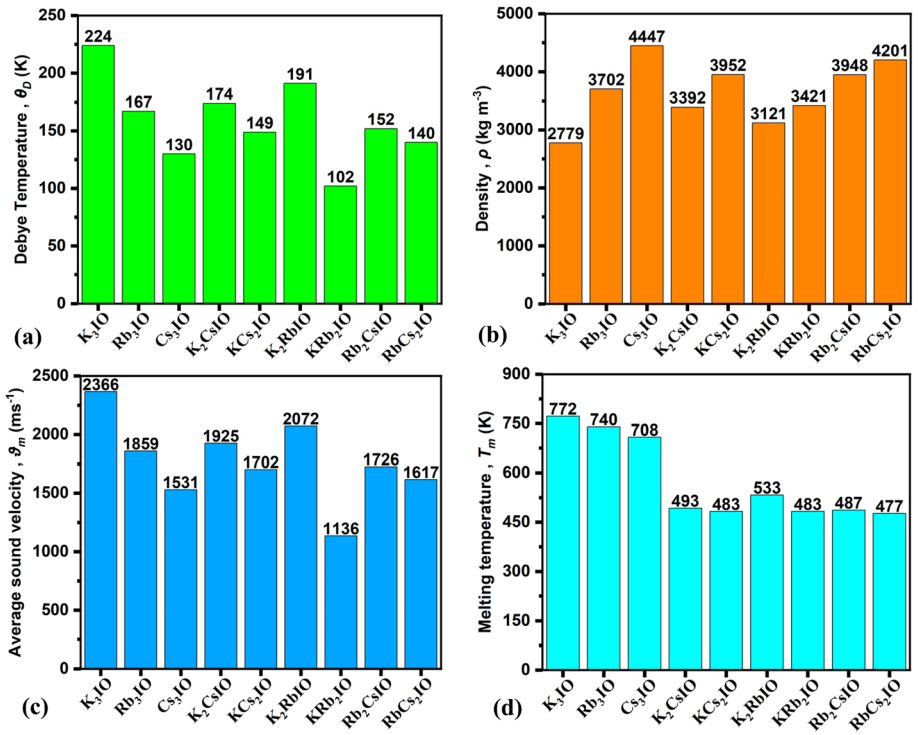

Fig. 10 Bar chart of Debye temperature (θ_D), crystal density (ρ), average sound velocity (ϑ_m), and melting temperature (T_m) of the pristine cubic structure K_3IO, Rb_3IO, and Cs_3IO; 33.33% doped tetragonal structure K_2CsIO, K_2RbIO, Rb_2CsIO; and 66.67% doped tetragonal structure KCs_2IO, KRb_2IO, and $RbCs_2IO$, respectively.

Table 6 Calculated Gruneisen parameter (Γ), specific heat (C_p, C_v) and thermal expansion coefficient (α) of the pristine cubic structure K_3IO, Rb_3IO, and Cs_3IO; 33.33% doped tetragonal structure K_2CsIO, K_2RbIO, Rb_2CsIO; and 66.67% doped tetragonal structure KCs_2IO, KRb_2IO, and $RbCs_2IO$, respectively

Compounds	Γ	C_p (J mol^{-1}K^{-1})	C_v (J mol^{-1}K^{-1})	α (10^{-5} K^{-1})
K_3IO (this work)	2.06	98	97	2.37
Rb_3IO (this work)	2.13	109	108	2.79
Cs_3IO (this work)	2.17	115	114	3.08
K_2CsIO (this work)	2.12	107	106	2.77
KCs_2IO (this work)	2.16	112	111	2.84
K_2RbIO (this work)	2.14	104	103	2.61
KRb_2IO (this work)	2.15	119	118	3.10
Rb_2CsIO (this work)	2.17	111	110	2.92
$RbCs_2IO$ (this work)	2.18	113	112	2.97

involve shear deformation and propagate through neighbouring atoms with lower restoring forces, this results in reduced wave energy and hence lower propagation speed.

Table 5 and Fig. 10 present the calculated sound velocities, mass densities, Debye temperatures, and melting temperatures of the studied compounds. The Debye temperature exhibits a decreasing trend as the A-site cation in the cubic structure is substituted from K to Rb and subsequently to Cs, as shown in Fig. 10(a). Consistent with this behaviour, the 66.67% doped structures display lower Debye temperatures compared to their corresponding 33.33% doped counterparts. Low θ_D effectively suppresses lattice thermal conductivity,[85] which is favourable for thermoelectric efficiency. This trend arises from the close dependence of the Debye temperature on the average sound velocity, which itself is strongly influenced by the material's mass density. A systematic increase in mass densities occurs as K is replaced by Rb and then Cs in the pristine cubic compounds. As a result, the 66.67% doped structures are denser than the corresponding 33.33% doped phases (Fig. 10(b)), which is expected to reduce sound velocities accordingly (Fig. 10(c)) and, consequently, lower the Debye temperature.

The melting temperatures (T_m) of the studied compounds reveal that the doped tetragonal structures generally melt at lower temperatures than the pristine cubic phases. The melting temperatures have been estimated using elastic-constant-based empirical relations:[86–88] $T_m = [553 + (5.911)\ C_{11}]$ for the cubic phase, and $T_m = [3C_{11} + 1.5C_{33} + 354]$ for the tetragonal phase. Fig. 10(d) shows that the melting temperature decreases as the A-site cation changes from K → Rb → Cs. Consistent with this trend, the 66.67% doped structures display lower T_m values compared to their corresponding 33.33% doped counterparts.

Among the doped structures, K_2RbIO achieved the highest melting point and the highest Debye temperature by A-site doping, which corresponds to the highest sound velocity and the lowest mass density. Overall, the doped tetragonal

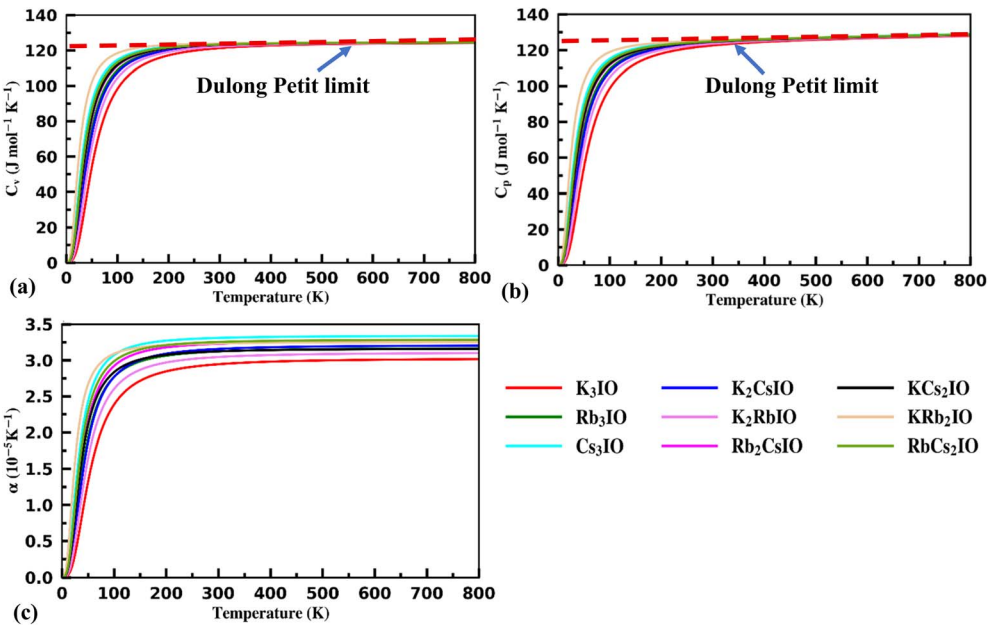

Fig. 11 Calculated specific heat at constant pressure and constant volume (C_p, C_v) and thermal expansion coefficient (α) of the pristine cubic structure K_3IO, Rb_3IO, and Cs_3IO; 33.33% doped tetragonal structure K_2CsIO, K_2RbIO, Rb_2CsIO; and 66.67% doped tetragonal structure KCs_2IO, KRb_2IO, and $RbCs_2IO$, respectively.

structures maintain lower T_m values than the pristine cubic compounds, indicating their distorted lattice atomic bond.

Specific heat at constant volume and constant pressure, and thermal expansion coefficient (listed in Table 6) have been calculated using the following equations:[89]

$$C_v = 9nN_Ak_B\left(\frac{T}{\theta_D}\right)\int_0^{x_D}\frac{e^x x^4}{(e^x-1)^2}dx; \quad \text{where } x_D = \frac{\theta_D}{T} \tag{22}$$

$$C_p = C_v(1 + \alpha\gamma T) \tag{23}$$

$$\alpha = \frac{\gamma C_v}{3BV}; \quad \text{where } B = \text{bulk modulus and } V = \text{molar volume} \tag{24}$$

The temperature dependence of the specific heat capacities at constant volume (C_v) and steady pressure (C_p) over the range 0–800 K is shown in Fig. 11(a and b). Both C_v and C_p increase with temperature due to thermal softening of the lattice. At temperatures below approximately 200 K, the heat capacities follow the Debye T^3 law, reflecting the dominance of low-frequency phonon modes. In contrast, at temperatures above about 300 K, the specific heat approaches the classical Dulong–Petit (DP) limit.[90] This confirms complete phonon activation from vibrational modes and lattice stability beyond room temperatures.[91,92] The thermal expansion coefficient (α) and its temperature dependence for all compounds are presented in Fig. 11(c). In all cases, α increases rapidly with temperature up to a characteristic range of approximately 0–200 K, beyond which it eventually approaches a near-constant value. For the cubic phases, α increases systematically as the A-site cation changes from K → Rb → Cs. Consequently, the 66.67% doped structures exhibit higher thermal expansion coefficients than their 33.33% doped counterparts.

3.5 Optical properties

The optical response of a material is largely determined by its electronic structure. The absorption coefficient, which is particularly important among other optical properties, quantifies the attenuation of incident light within the material. The effect of A-site doping on the optical behaviour of $A_{3-x}A'_xIO$ (A = K, Rb, Cs) has been highlighted in this section.

3.5.1 Dielectric function (ε). The dielectric function refers to the optical response of solids. In this work, both the real part, $\varepsilon_1(\omega)$, and the imaginary part, $\varepsilon_2(\omega)$, of the dielectric function is analysed. The $\varepsilon_1(\omega)$ component is related to the polarisation effects and the propagation of electromagnetic waves within the material. Additionally, $\varepsilon_2(\omega)$ emphasis on the material's absorption properties.[93] The imaginary ε_2 and real (ε_1)

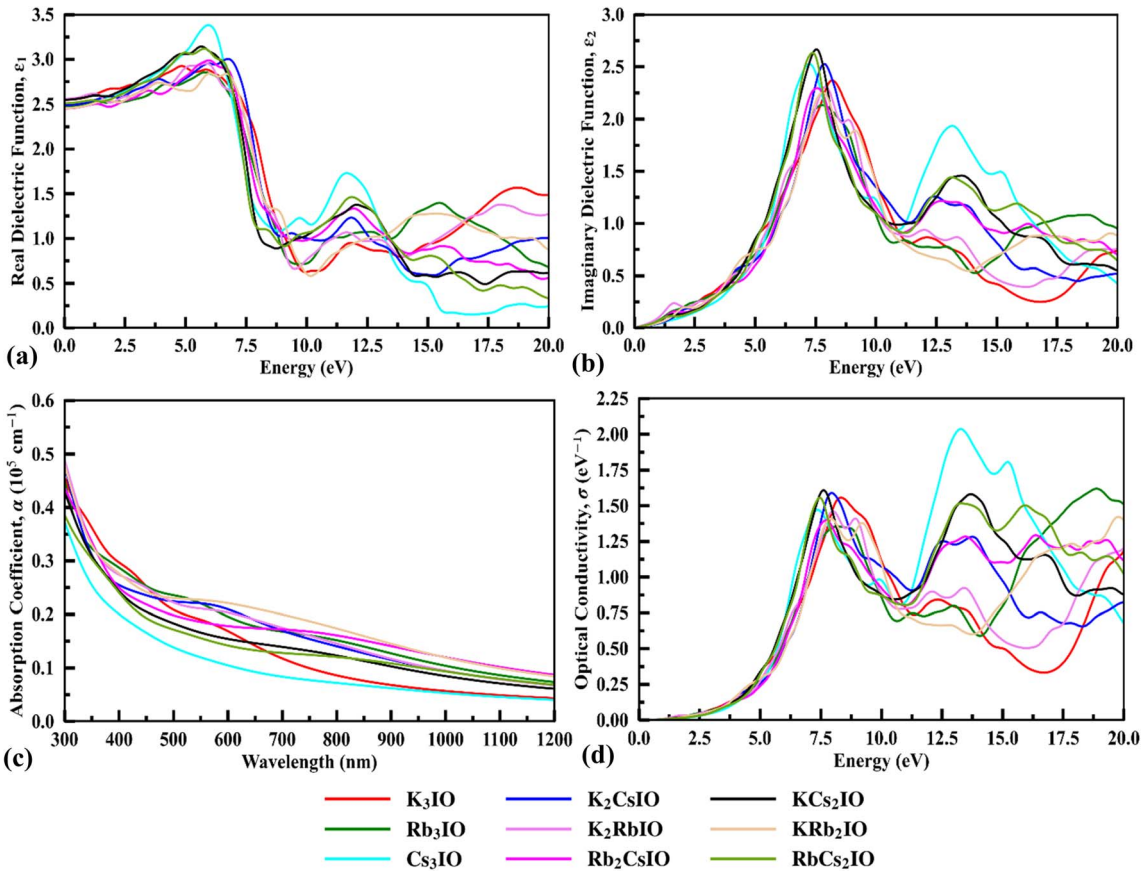

Fig. 12 Calculated real (ε_1) and imaginary (ε_2) components of the dielectric function, absorption coefficient (α), and optical conductivity (σ) of the pristine cubic structure K_3IO, Rb_3IO, and Cs_3IO; 33.33% doped tetragonal structure K_2CsIO, K_2RbIO, Rb_2CsIO; and 66.67% doped tetragonal structure KCs_2IO, KRb_2IO, and $RbCs_2IO$, respectively.

components of the dielectric function are calculated using the following equations:[94]

$$\varepsilon_2(\omega) = \frac{2e^2\pi}{\Omega\varepsilon_0}\sum_{k,V,C}\left|\left\langle\psi_k^C\left|\vec{U}\cdot\vec{r}\right|\psi_k^V\right\rangle\right|^2\delta\left(E_k^C - E_k^V - E\right) \quad (25)$$

$$\varepsilon_1(\omega) = 1 + \frac{2}{\pi}P\int_0^\infty \frac{\omega'\varepsilon_2(\omega)'}{\omega'^2 - \omega'}\mathrm{d}\omega' \quad (26)$$

In these expressions, e denotes the electronic charge and Ω represents the unit cell volume. The quantities ${\Psi_k}^V$ and ${E_k}^V$ correspond to the valence-band wave functions and energies at a given k-point, while ${\Psi_k}^C$ and ${E_k}^C$ represent their counterparts in the conduction band. The vector U also defines the polarisation direction of the electric field associated with the incoming light.

The real and imaginary components of the calculated dielectric function are presented in Fig. 12(a), over an energy range of 0–20 eV. The real part of the dielectric function reflects the material's ability to store electromagnetic energy. For all studied compounds, the maximum value of ε_1 occurs within the energy range of 5.0 to 6.25 eV. The magnitude of ε_1 follows the order: pristine Cs_3IO > 66.67% Cs-doped structures (KCs_2IO and $RbCs_2IO$) > 33.33% Cs-doped structure (K_2CsIO and Rb_2CsIO) > pristine K_3IO > 33.33% and 66.67% Rb-doped structure (K_2RbIO and KRb_2IO) > pristine Rb_3IO. This trend indicates that Cs substitution has the most pronounced effect on enhancing the energy storage capability of K_3IO and Rb_3IO anti-perovskites. Rb substitution also produces a noticeable, though comparatively smaller enhancement.

The imaginary part of the dielectric function, ε_2, is directly associated with optical absorption within the crystal and arises from electronic transitions between occupied and unoccupied energy bands.[95] Peaks in ε_2 correspond to interband transitions from the valence band to the conduction band and are closely linked to the electronic band structure. As shown in Fig. 12(b), ε_2 remains zero until the photon energy reaches the band gap of each phase; after that, it increases sharply. The 66.67% Cs-doped structures (KCs_2IO and $RbCs_2IO$, ~2.55) have shown the highest ε_2 values. Overall, ε_2 exhibits a pronounced primary peak in the 6–9 eV range for all compositions, which is in the UV range. This phenomenon can be attributed as transitions of electrons from O-2p and I-5p dominated valence states to alkali (K-4s, Rb-5s, Cs-6s) conduction states, as shown in Fig. 7. Mixed-alkali tetragonal phases display broader ε_2 features, indicating enhanced transition channels due to symmetry lowering and band-edge disorder.

3.5.2 Absorption coefficient (α). The absorption coefficient quantifies the attenuation of light as it propagates through a material.[96] This behaviour is governed by the electronic band gap and the atomic structure. At the microscopic level, optical absorption occurs when the energy of incident photons matches the allowed electronic transition energies. As a result, materials absorb light preferentially at specific frequencies, and the absorption coefficient varies accordingly with photon energy. The following equation has been used to calculate the $\alpha(\omega)$:[97]

$$\alpha(\omega) = \frac{2\omega}{c}\left[\left(\varepsilon_1(\omega)^2 + \varepsilon_2(\omega)^2\right)^{\frac{1}{2}} - \varepsilon_1(\omega)\right]^{\frac{1}{2}}. \quad (27)$$

All studied compounds exhibit absorption coefficients on the order of 10^5 cm^{-1} within the visible region, as shown in Fig. 12(c). The magnitude of the absorption coefficient in the visible spectrum follows the sequence (~0.3×10^5 cm^{-1}): 33.33% and 66.67% Rb-doped structure (K_2RbIO and KRb_2IO) > pristine Rb_3IO > 33.33% Cs-doped structure (K_2CsIO and Rb_2CsIO) > pristine K_3IO > 66.67% Cs-doped structures (KCs_2IO and $RbCs_2IO$) > pristine Cs_3IO. This trend describes the influence of Rb substitution on enhancing the optical absorption of the $A_{3-x}A'_xIO$ anti-perovskites. Because of the good absorption coefficient in the visible spectrum range, the studied compounds can be used as a potential absorber layer in single-junction solar cells.

3.5.3 Optical conductivity (σ). The optical conductivity spectra, shown in Fig. 12(d), exhibit a sharp increase beyond approximately 5 eV, followed by pronounced peaks in the 7–9 eV range, which are associated with strong inter-band transitions in the UV range. Mathematically, the optical conductivity can be expressed as follows:[98]

$$\sigma(\omega) = -\frac{i\omega}{4\pi}\varepsilon(\omega) \quad (28)$$

The overall maximum $\sigma(\omega)$ values follow the order (within UV range): pristine Cs_3IO > 66.67% Cs-doped structures (KCs_2IO and $RbCs_2IO$) > 33.33% Cs-doped structures (K_2CsIO and Rb_2CsIO) > pristine K_3IO > 33.33% and 66.67% Rb-doped structures (K_2RbIO and KRb_2IO) > pristine Rb_3IO. This behaviour indicates that $\sigma(\omega)$ is generally higher for Cs-doped compounds, which can be associated with their higher polarizability, as mentioned in the charge density Section 3.2.3. The mixed A-site compositions show a broader range of conductivity spectra due to the presence of disorder-related electronic states, as mentioned in the PDOS section.

3.5.4 Reflectivity (R). When light is incident on the surface of a material, or at the boundary between two different media, a portion of it returns to the original medium. This phenomenon is known as reflectivity. Fig. 13(a) shows the reflectivity of the studied compounds, which have been calculated using the following equation:[97]

$$R(\omega) = \frac{(n-1)^2 + k^2}{(n+1)^2 + k^2} \quad (29)$$

Here, n and k represent the real and imaginary parts of the refractive index, respectively. The highest reflectivity remains relatively low, below 15%, across the investigated energy range of 0–20 eV. Within the range, 5% reflectivity has been observed within the visible range. It indicates minimal metallic character and favourable transparency at low photon energies. The overall low reflectivity highlights the potential of these materials for

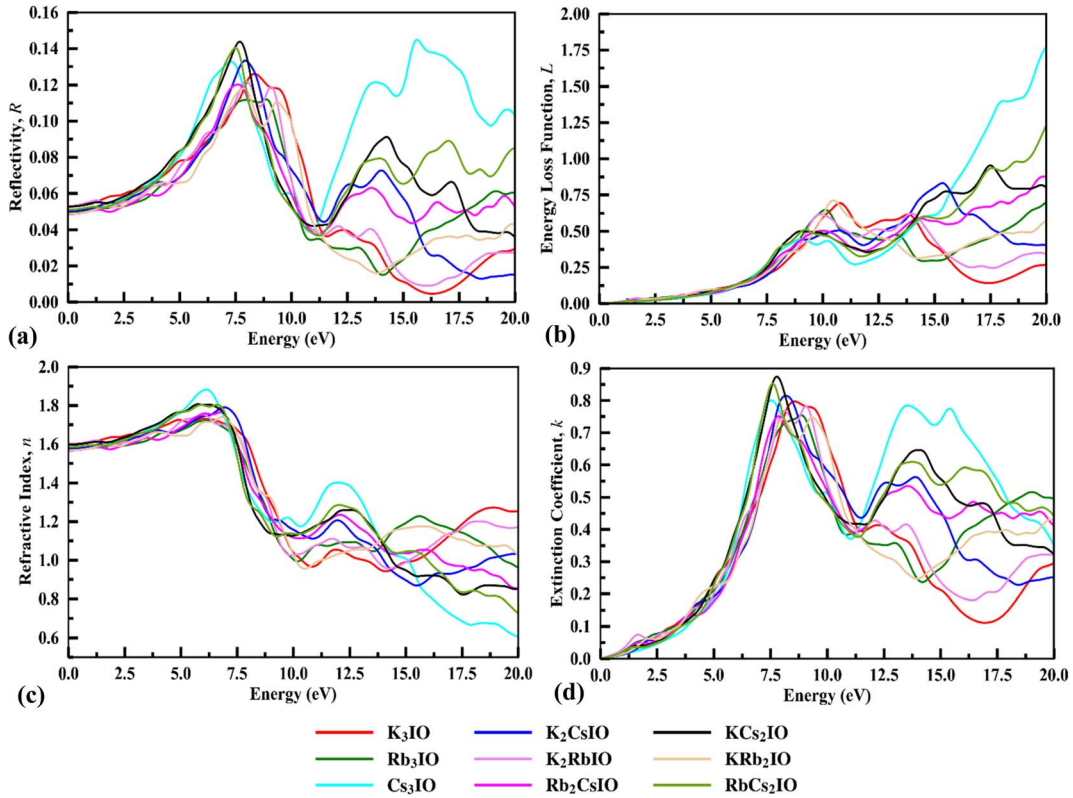

Fig. 13 Calculated reflectivity (R), energy loss function (L), refractive index (n), and extinction coefficient (k) of the pristine cubic structure K_3IO, Rb_3IO, and Cs_3IO; 33.33% doped tetragonal structure K_2CsIO, K_2RbIO, Rb_2CsIO; and 66.67% doped tetragonal structure KCs_2IO, KRb_2IO, and $RbCs_2IO$, respectively.

use as anti-reflective coatings and light-absorbing layers in solar cell applications.

3.5.5 Loss function (L). The electron energy loss function, $L(\omega)$, is a key quantity for probing the optical response of materials, as it describes the energy dissipation of fast electrons traversing a solid. Energy losses arise from electronic excitations, and plasmonic features are directly reflected in the $L(\omega)$ spectra. Fig. 13(b) shows the energy loss functions of the studied compounds, which are calculated using the following formula:[97]

$$L(\omega) = \frac{\varepsilon_2(\omega)}{\varepsilon_1(\omega)^2 + \varepsilon_2(\omega)^2}. \quad (30)$$

Well-defined plasmon resonance peaks appear at higher energies, above approximately 10 eV in the UV-range, indicating collective oscillations of the valence electrons. These plasmon peaks shift slightly toward lower energies in the Cs and Rb-doped systems. This finding is consistent with enhanced electronic polarizability and a corresponding reduction in plasmon energies. Besides these, all the studied compounds show very small energy loss within the visible spectrum.

3.5.6 Refractive index (n) and extinction coefficient (k). The refractive index, $n(\omega)$, and the extinction coefficient, $k(\omega)$, provide insight into the propagation speed of photons in a material and its light absorption efficiency,[99] which have been calculated using the following formula:[97]

$$n(\omega) = \frac{1}{\sqrt{2}}\left[\left(\varepsilon_1(\omega)^2 + \varepsilon_2(\omega)^2\right)^{\frac{1}{2}} + \varepsilon_1(\omega)\right]^{\frac{1}{2}}. \quad (31)$$

$$k(\omega) = 1 + \frac{1}{\sqrt{2}}\left[\left(\varepsilon_1(\omega)^2 + \varepsilon_2(\omega)^2\right)^{\frac{1}{2}} - \varepsilon_1(\omega)\right]^{\frac{1}{2}}. \quad (32)$$

For the studied compounds, the refractive index is shown in Fig. 13(c), which is similar to the real part of the dielectric function over the entire energy range. This behaviour reflects the close connection between the optical response and the electronic structure. All compounds exhibit similar static refractive index values, with $n(0) \approx 1.6$. As commonly observed in semiconductors, materials with wider band gaps tend to show lower static refractive indices.[98] Accordingly, K_3IO, which has the widest band gap, shows the smallest refractive index. In contrast, Cs and Rb-doped structures exhibit higher n values due to their reduced band gaps, following the same doping effects observed for the real part of the dielectric function.

The extinction coefficient, $k(\omega)$, of the studied compounds is also presented in Fig. 13(d). For all materials, $k(\omega)$ remains zero within the band gap region, indicating the absence of optical

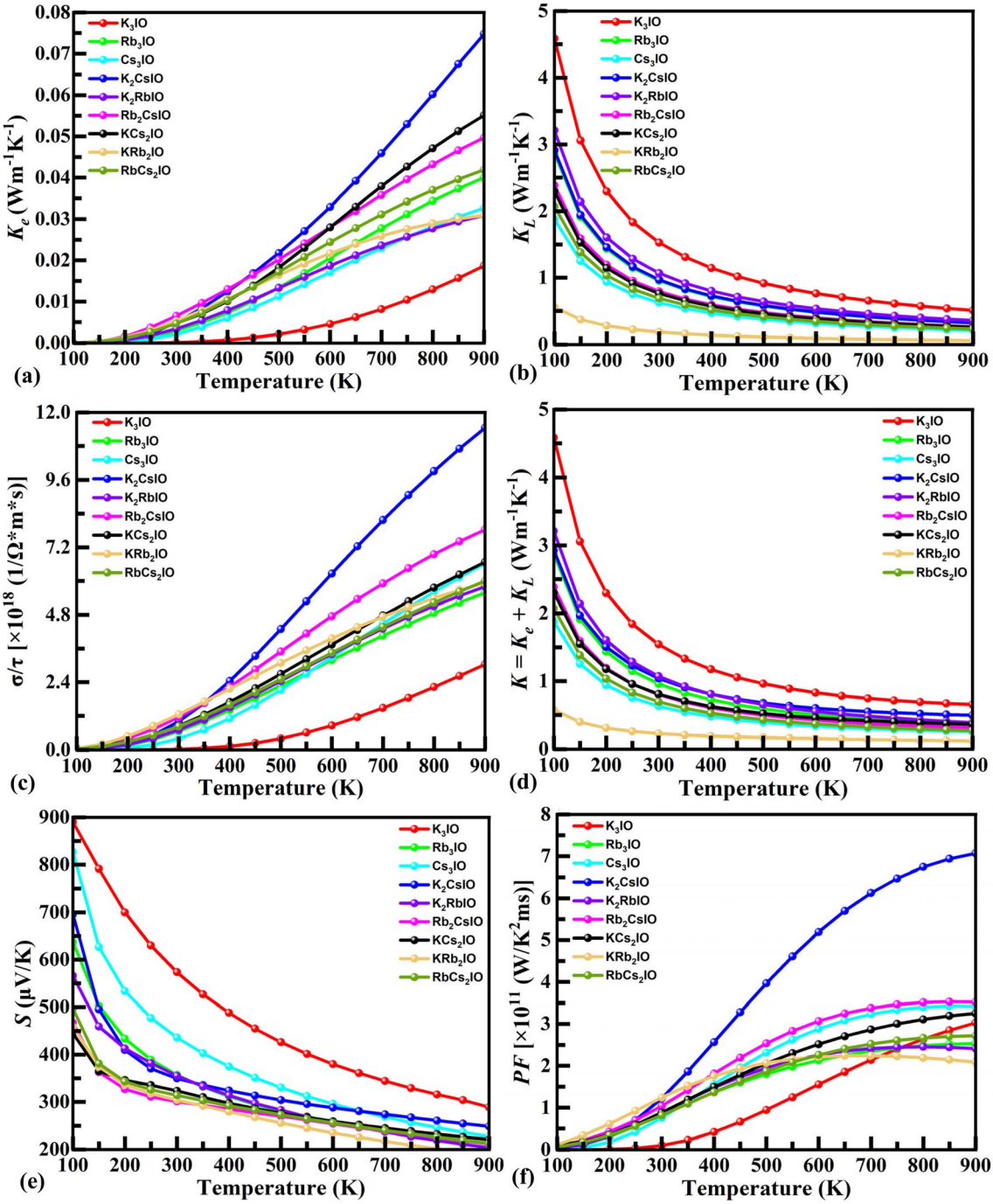

Fig. 14 Calculated electronic thermal conductivity (K_e), lattice thermal conductivity (K_L), total thermal conductivity (K), electrical conductivity (σ/τ), Seebeck coefficient (S) and power factor (PF) of the pristine cubic structure K_3IO, Rb_3IO, and Cs_3IO; 33.33% doped tetragonal structure K_2CsIO, K_2RbIO, Rb_2CsIO; and 66.67% doped tetragonal structure KCs_2IO, KRb_2IO, and $RbCs_2IO$, respectively.

absorption at low photon energies. Once the photon energy exceeds the band gap, $k(\omega)$ increases sharply and reaches its maximum in the energy range of approximately 7–10 eV. The overall spectral features and doping effects of $k(\omega)$ closely follow those of the imaginary part of the dielectric function. Compared to the pristine phases, the Cs and Rb-doped structures exhibit enhanced $k(\omega)$ values, indicating stronger optical absorption at higher energies.

3.6 Thermoelectric properties

Thermoelectric properties define a material's ability to convert a temperature gradient into an electrical response. This property forms the foundation of power generation, cooling, and temperature sensing in thermoelectric devices.[100] To estimate the thermoelectric performance of the studied compounds, the electronic thermal conductivity (K_e), lattice thermal

conductivity (K_L), total thermal conductivity (K), electrical conductivity (σ/τ), Seebeck coefficient (S), power factor (PF), and the dimensionless figure of merit (ZT)[101] have been assessed. These quantities are calculated using the Boltzmann transport equation by the BoltzTrap2 code[49] within the constant relaxation time, τ of 10^{-15} s. However, incorporating the higher-order anharmonicity can improve the accuracy of the calculations. All the thermoelectric parameters are evaluated over a temperature range of 100–900 K.

3.6.1 Thermal conductivity (K). Thermal conductivity describes a material's ability to transport heat. The total thermal conductivity (K) consists of two contributions: the lattice thermal conductivity (K_L), arising from lattice vibrations, and the electronic thermal conductivity (K_e), associated with the transport of charge carriers. As shown in Fig. 14(a), the K_e of all studied compounds increases monotonically with temperature. This behaviour indicates that higher temperatures thermally excite a larger number of charge carriers, enhancing their mobility and thereby promoting heat transport. Among the investigated materials, the Cs-doped tetragonal phases generally exhibit higher K_e values than their parent cubic compounds K_3IO and Rb_3IO. The Rb-doped tetragonal structures also show higher K_e than the parent K_3IO. This is consistent with the doped structure's reduced band gaps, which results relatively higher carrier concentrations. At the elevated temperature, the overall trend in K_e follows the sequence: 33.33% and 66.67% Cs-doped K_3IO (K_2CsIO and KCs_2IO) > 33.33% and 66.67% Cs-doped Rb_3IO (Rb_2CsIO and $RbCs_2IO$) > pristine Rb_3IO >33.33% and 66.67% Rb-doped K_3IO (K_2RbIO, KRb_2IO) > pristine Cs_3IO > pristine K_3IO.

The temperature-dependent lattice thermal conductivity, K_L, is evaluated using the following Slack equation:[102]

$$K_L = \frac{A\theta_D{}^3 V^{\frac{1}{3}} m}{\gamma^2 N^{\frac{2}{3}} T}. \quad (33)$$

Here θ_D, γ, V, m, N and T represents the Debye temperature, Gruneisen parameter, molar volume, average molar mass per atom, number of atoms in the unit cell, and the absolute temperature, respectively. In equation,[33] A is a constant with a value of 3.04×10^{-8}.

As shown in Fig. 14(b), K_L exhibits an inverse relationship with temperature for all compositions, decreasing steadily as the temperature increases. This behaviour can be ascribed to the reduced contribution of phonons to heat transport at higher temperatures, where phonon–phonon scattering becomes more significant.[103] The K_L values follow the sequence: pristine K_3IO > 33.33% Rb-doped K_3IO (K_2RbIO) > 33.33% Cs-doped structures (K_2CsIO and Rb_2CsIO) > 66.67% Cs-doped structures (KCs_2IO and $RbCs_2IO$) > pristine Rb_3IO > pristine Cs_3IO > 66.67% Rb-doped K_3IO (KRb_2IO). This trend is governed by the combined effects of atomic mass, lattice symmetry, and alloy-induced phonon scattering.[104]

Fig. 14(d) presents the total thermal conductivity, $K = K_e + K_L$, which includes combined contributions from both phonons and charge carriers. The overall thermal conductivity remains relatively low and is largely governed by the lattice component, K_L, which decreases with increasing temperature. Compared with the pristine cubic phases, the doped structures therefore exhibit a stronger suppression of heat transport. Specifically, KRb_2IO has shown the lowest thermal conductivity, which results in the highest ZT at room temperature. The reduced lattice contribution (K_L), together with a finite electronic contribution (K_e), favours the retention of a temperature gradient across the material, which is relevant for thermoelectric performance.

3.6.2 Electrical conductivity (σ/τ). Electrical conductivity describes a material's ability to transport charge carriers. The temperature dependence of σ/τ is shown in Fig. 14(c). For all studied compounds, σ/τ increases steadily with temperature, reflecting the semiconducting behaviour. This trend arises from the thermally activated increase in carrier concentration, while the overall conductivity follows the relation: $\sigma = n \times e \times \mu$. Here, n, e, and μ represent the carrier concentration, elementary charge, and the carrier mobility, respectively. At low temperatures, the materials exhibit limited electrical conduction. As the temperature rises, thermal energy energies electrons from the valence band to the conduction band, which generates electron–hole pairs and ultimately increases the carrier concentration. The efficiency of this thermal activation depends on the band gap of each compound, where wider band gaps require higher excitation energies.

Among the studied anti-perovskites, K_2CsIO exhibits the highest electrical conductivity, reaching $1.2 \times 10^{18}\ \Omega^{-1}\ m^{-1}\ s^{-1}$ at the room temperature (300 K). This enhanced conductivity arises from its relatively small band gap, which facilitates more efficient charge-carrier generation. For comparison, other inorganic thermoelectric perovskites such as $CsSnBr_3$ and $CsSnI_3$ show electrical conductivity of $1.7 \times 10^{17}\ \Omega^{-1}\ m^{-1}\ s^{-1}$ and $2.9 \times 10^{19}\ \Omega^{-1}\ m^{-1}\ s^{-1}$ (ref. 105) at room temperature, respectively, while their mixed-halide counterparts $CsSnBr_{3-x}I_x$ (x = 0, 0.5, 1, 2 and 3) show intermediate σ/τ values.[105] These comparisons indicate that doping with Cs and Rb plays a crucial role in tuning the electrical conductivity through band-gap modulation.

3.6.3 Seebeck coefficient (S). Thermoelectric materials generate an electrical voltage when subjected to a temperature gradient, which can be described by the Seebeck effect. This phenomenon is quantified by the Seebeck coefficient (S), defined through the relation $\Delta V = S\Delta T$, where ΔV and ΔT represent the generated voltage and the applied temperature difference, respectively. The magnitude of S depends on the charge-carrier transport and scattering processes within the material. Other inorganic perovskites like $CsSnBr_{3-x}I_x$ (x = 0, 0.5, 1, 2 and 3) have an S value of 325, 269, 156, 99, 48 $\mu V\ K^{-1}$, respectively, at room temperature.[105] Here, the value of S decreased due to the halide-site doping. A similar trend has been observed in the studied $A_{3-x}A'_xIO$ (A/A′ = K, Rb, Cs) anti-perovskites, where A-site doping decreases the S value (Fig. 14(e)). At room temperature, the S trend follows: pristine compounds K_3IO, Cs_3IO and Rb_3IO (~580, 450 and 380 $\mu V\ K^{-1}$), respectively > 33.33% doped structures K_2CsIO, K_2RbIO and Rb_2CsIO (~350–300 $\mu V\ K^{-1}$) > 66.67% doped structures KCs_2IO, KRb_2IO and $RbCs_2IO$ (~300 $\mu V\ K^{-1}$).

Fig. 14(e) shows the temperature dependence of the S for the studied compounds. All materials exhibit positive S across the entire temperature range, indicating dominant p-type charge transport. The magnitude of S decreases as the temperature increases, representing semiconducting behaviour. As thermal energy increases, electrons become excited from the valence band to the conduction band and generate electron–hole pairs. As a result, the carrier concentration increased which leads to a reduction in S, as $S \propto \frac{m^* T}{n^{\frac{2}{3}}}$,[106] where m^*, n, and T represent the effective mass of charge carriers, charge carrier concentration, and the absolute temperature, respectively. The compounds that show larger S at low temperatures, such as pristine K_3IO, can be attributed to their wider band gaps and lower intrinsic carrier concentrations.

3.6.4 Power factor (PF). The power factor (PF) measures a material's capability of converting thermal energy into electrical energy. It represents the electrical contribution to thermoelectric performance through the combined influence of the Seebeck coefficient and electrical conductivity, which is defined as $PF = S^2(\sigma/\tau)$.

For all studied compositions, the PF increases with rising temperature. This enhancement occurs due to the combined effect of rising σ and the moderate retention of S at elevated temperatures. Among the studied compounds, K_2CsIO exhibits the highest PF, reaching values of 4×10^{11} W m^{-1} K^{-2} s^{-1} at its melting temperature (493 K), as shown in Fig. 14(f). For comparison, a promising inorganic thermoelectric perovskite $CsSnI_3$ achieves PF of 1.86×10^{11} W m^{-1} K^{-2} s^{-1} at room temperature,[107] whereas K_2CsIO also exhibits similar PF at 300 K. Other Cs and Rb-doped structures also show good PF of (1–1.5) $\times 10^{11}$ W m^{-1} K^{-2} s^{-1}, at room temperature, which may be considered as potential candidates for low temperature thermoelectric applications. In contrast, the cubic compounds show comparatively lower PF values, primarily due to their reduced σ. The superior PF observed in the mixed-alkali tetragonal structures reflects the importance of alkali-site engineering as an effective strategy for enhancing the overall thermoelectric efficiency.

3.6.5 Figure of merit (*ZT*). The thermoelectric efficiency of a material is commonly quantified using the dimensionless figure of merit, ZT, which is defined as: $ZT = \frac{S^2 \sigma T}{\kappa}$.[108] A material is generally considered suitable for practical thermoelectric applications when ZT approaches or exceeds unity. Higher ZT values correspond to improved efficiency in converting thermal energy into electrical energy. Enhancement of ZT can be achieved through an increase in the Seebeck coefficient and electrical conductivity, or by reducing the total thermal conductivity (K). Since ZT reflects the balance between electrical transport and heat dissipation, maximising this parameter requires simultaneously promoting charge carrier transport while suppressing phonon-mediated heat conduction. Consequently, materials exhibiting large ZT values demonstrate superior performance in thermoelectric energy conversion applications.

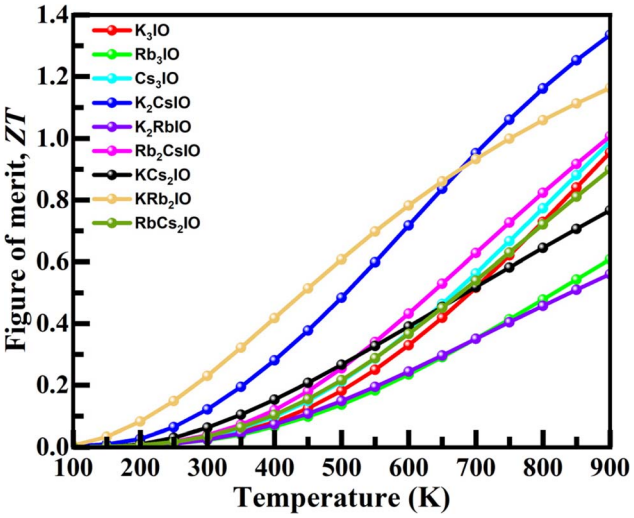

Fig. 15 Calculated figure of merit (ZT) of the pristine cubic structure K_3IO, Rb_3IO, and Cs_3IO; 33.33% doped tetragonal structure K_2CsIO, K_2RbIO, Rb_2CsIO; and 66.67% doped tetragonal structure KCs_2IO, KRb_2IO, and $RbCs_2IO$, respectively.

The temperature dependence of the ZT for all nine $A_{3-x}A'_xIO$-based compounds is presented in Fig. 15. For every composition, ZT increases monotonically with temperature, confirming that these materials are better suited for intermediate to high temperature thermoelectric applications. This behaviour arises from the combined enhancement of the power factor and the concurrent reduction of lattice thermal conductivity at elevated temperatures.

Among the pristine cubic phases, Cs_3IO exhibits the highest ZT value (0.6) at the T_m ~708 K. The reason can be attributed to its relatively narrow band gap, higher electrical conductivity, and comparatively lower total thermal conductivity.[109] Substituting Cs and Rb within K_3IO and Rb_3IO systematically improves the thermoelectric performance. KRb_2IO and K_2CsIO exhibit the highest ZT of 0.5 and 0.6, respectively, at their melting point (T_m ~490 K). This improvement is mainly associated with bandgap narrowing and the resulting increase in carrier concentration, which enhances electrical conductivity while maintaining a reasonable Seebeck coefficient. Comparing with the ZT values of some other inorganic perovskites, such as $CsGeI_3$ (1.05), $CsSnI_3$ (0.95), and $CsPbI_3$ (0.45) at 700 K,[110] the studied anti-perovskites show better thermoelectric performance.

The remaining mixed compositions, including KCs_2IO, Rb_2CsIO, and $RbCs_2IO$, also demonstrate higher ZT values than the cubic phases. Although their power factors are slightly lower, their reduced lattice thermal conductivity ensures a steady increase in ZT with temperature. These results indicate that alkali-metal substitution and the associated symmetry lowering from cubic to tetragonal structures are effective in improving the thermoelectric properties of the studied $A_{3-x}A'_xIO$-based compounds. Furthermore, the thermoelectric trends reported in this study are governed by well-understood mechanisms such as band-gap tuning, mass disorder, and lattice softening. These trends are

consistent with experimentally observed behaviour in related perovskite and thermoelectric materials. For example, Khan *et al.* demonstrated that the Boltzmann transport equation and slack model-based thermoelectric calculations of oxide-based perovskites have closely matched *ZT* with experiment.[111] The *ZT* ratio of experimental value and theoretically calculated value for doped $CaTiO_3$ and doped $SrTiO_3$ is 0.4/0.45 and 0.64/0.68, respectively.[111] Therefore, the method used in this study is reliable and widely used to calculate the thermoelectric properties.

4 Conclusion

In this work, a comprehensive first-principles and molecular dynamics investigation of alkali-metal doped $A_{3-x}A'_xIO$ (A/A′ = K, Rb, Cs) anti-perovskites have been studied. The aim is to elucidate the impact of larger alkali-metal substitution and doping on their physical properties. The findings of this work establish that alkali-site doping is an effective strategy for tuning the electronic, mechanical, optical, thermal, and thermoelectric behaviour of anti-perovskite materials. In particular, alkali-site doping significantly reduces the direct band gap into the optimal range for photovoltaic applications, which improves the Shockley–Queisser limit efficiency. The doping simultaneously enhances optical absorption and suppresses reflectivity in the visible region. Mechanical property analysis reveals that site-doped compounds exhibit improved ductility and machinability compared to pristine structures, indicating better structural reliability for device fabrication. KCs_2IO shows the highest ductility, with a Pugh's ratio of 1.67, and KRb_2IO achieves the highest machinability, with an index value of 2.08. Thermal properties show that among the studied site-doped compositions, K_2RbIO possess the highest Debye temperature (191 K) and melting point (533 K). Moreover, the thermoelectric performance is notably enhanced in K_2CsIO and KRb_2IO. Importantly, some studied compounds (Cs_3IO, KRb_2IO and $RbCs_2IO$) show phonon instability at 0 K, which remain stable at room temperature. Similar phenomena can be found in the literature, where several synthesized perovskites, such as $BaTiO_3$,[112] $SrTiO_3$,[113] and $MAPbBr_3$,[114] exhibit imaginary phonon modes at 0 K. Additionally, stable AIMD output confirms the thermal stability of the studied anti-perovskites. Compared to Si and CIGS absorbers in solar cells, the studied anti-perovskites rely primarily on earth-abundant and low-cost alkali elements, and avoid critical elements such as In, Ga, Se, and Te that dominate high-performance photovoltaic and thermoelectric materials. It may also minimise the dependence on scarce tellurides and selenides, which can significantly reduce material cost and supply-risk concerns. Overall, this work establishes that alkali-metal A-site doping enables the pristine anti-perovskites to have dual application, both in a single-junction solar cell and in thermoelectric applications.

Author contributions

Kashfi Uddin: writing – original draft, writing – review & editing, visualization, validation, methodology, investigation, formal analysis, data curation, conceptualization. Abu Sadat Md. Sayem Rahman: writing – review & editing, supervision, resources, visualization, validation, methodology, investigation, formal analysis, conceptualization.

Conflicts of interest

There are no conflicts of interest to declare.

Data availability

Data for this article, including structural, electronic, mechanical, thermal, optical, and thermoelectric properties data, are available at zenodo repository at https://doi.org/10.5281/zenodo.18662841.

Acknowledgements

The authors are thankful to the Department of Materials and Metallurgical Engineering, CUET, for providing the computational lab facility during the simulation work. The authors also gratefully acknowledge Dr Paolo Giannozzi, Dr Pietro Delugas and the Quantum Espresso Foundation for providing free access to the Quantum Espresso simulation software.

References

1 *Interactive Best Research-Cell Efficiency Chart*, https://www.nrel.gov/pv/interactivecell-efficiency, Dec. 6, 2025.
2 K. Uddin and A. S. M. S. Rahman, Design of lead-free triple-absorber perovskite/ACIGS 2T tandem solar cell: Machine learning and SCAPS-1D approach, *J. Phys. Chem. Solids*, 2026, **210**, 113350, DOI: 10.1016/j.jpcs.2025.113350.
3 N. Dengo, D. F. Macias-Pinilla, S. Virga, S. Bini, F. Giannici and F. Bertolotti, Bonding Mechanisms Underpinning Structural and Electronic Properties of Halide Perovskites, *Coord. Chem. Rev.*, 2026, **552**, 217470, DOI: 10.1016/j.ccr.2025.217470.
4 X. Zhao, H. Li, H. Li, T. Dong, J. Li, Z. Li, *et al.*, Boosting the Efficiency and Stability of Perovskite Solar Cells *via* A-Site Quintuple-Cation Engineering, *ACS Appl. Energy Mater.*, 2026, **9**(1), 584–592, DOI: 10.1021/acsaem.5c03375.
5 Z. Zhang, Y. Cui, G. Chen, H. Zhou, X. Wang, J. Feng, *et al.*, Enhancing the Efficiency and Stability of CsFA-Based Perovskite Solar Cells: Defect Passivation Using Indoline-Based D–π–A Configured Molecule as Additive, *Prog. Photovolt.: Res. Appl.*, 2026, **34**(2), 161–170, DOI: 10.1002/pip.3920.
6 M. S. Ali, R. Parvin, M. Sabah, M. S. Islam, M. T. Ahmed, M. H. Rahman, *et al.*, Investigation of structural, mechanical, electronic, and optical properties of anti-perovskite solid electrolyte R_3OX (R = Li, Na and X = Cl, Br), *Phys. B*, 2026, **725**, 418183, DOI: 10.1016/j.physb.2025.418183.
7 Yuvraj, Review on Theoretical Exploration of Low-Dimensional Anti-Perovskite Nanostructures and Their Stability, *J. Sci. Innovations Nat. Earth*, 2025, **5**(2), 60–62, DOI: 10.59436/jsiane.388.2583-2093.

8 Y. Hu, S. Zhao and L. Chen, Prediction of Ruddlesden–Popper Antiperovskites K_4OBr_2 and K_4OI_2 for Potential Thermoelectric Application, *J. Phys. Chem. C*, 2025, **129**(9), 4656–4663, DOI: 10.1021/acs.jpcc.4c07834.

9 A. Ayyaz, Q. Mahmood, S. K. Ali, M. Naeem, L. G. Amin, M. B. Shakir, *et al.*, DFT Evaluation of Physical Characteristics of Novel Antiperovskites K_3CuO and K_3AgO for Optoelectronic and Thermoelectric Technologies, *J. Inorg. Organomet. Polym. Mater.*, 2025, **35**(4), 2697–2708, DOI: 10.1007/s10904-024-03414-8.

10 Y. Zhang, Y. Du, X. Liu, F. Zhang, C. Kang and J. Tian, *et al. Collaborative Regulations of Phase Transition for Enhancing Negative Thermal Expansion of $Mg_2P_2O_7$ by Lattice Stress and Charge Repulsion Force*. 2025. DOI: 10.2139/ssrn.5213001.

11 A. Ayyaz, M. Zaman, I. Boukhris, O. Zayed, T. M. Al-Daraghmeh, S. Bouzgarrou, *et al.*, First-Principles Calculations to Investigate Structural, Mechanical, Electronic, and Optical Properties of Inverse Perovskite Oxides X_3AuO (Li, Na, K): Stable and Sustainable Materials for Photovoltaic Applications, *J. Inorg. Organomet. Polym. Mater.*, 2025, **35**(11), 9491–9506, DOI: 10.1007/s10904-025-03872-8.

12 MdR. Hossain, K. M. Shamima, P. Mondal, A. K. Paul and F. Ahmed, Compositional tuning and property evolution in cubic Mg-based perovskite and anti-perovskite compounds ($MgBO_3$ and Mg_3BO; B = Si, Ge, Sn, Pb): a comparative first-principles study for multifunctional device applications, *Mater. Adv.*, 2026, **7**(1), 618–640, DOI: 10.1039/D5MA00961H.

13 R. Rafiu, MdS. Hasan Saikot, I. A. Apon, I. Boukhris, A. El-Rayyes, M. T. Khan, *et al.*, Comprehensive DFT and SCAPS-1DStudy of Structural, Electronic, Optical, Mechanical, Phonon, Thermoelectric, and Photovoltaic Properties of Lead-Free Z_3BrO (Z = K, Rb, Cs, and Fr) Anti-Perovskites, *J. Comput. Chem.*, 2025, **46**(24), DOI: 10.1002/jcc.70221.

14 A. C. Garcia-Castro, Interplay between the B -sites' valence states and phonon dynamics in the Ca_3BO (B=Si, Ge, Sn, and Pb) antiperovskites, *Solid State Commun.*, 2025, **401**, 115898.

15 A. Vijay, S. Charan Prasanth, R. Jose and K. Venkata Saravanan, Synthesis of n-type $CaMnO_3$ and its A-site doped derivatives for thermoelectric applications, *Phys. Scr.*, 2026, **101**(1), 015908, DOI: 10.1088/1402-4896/ae3038.

16 S. O. A. Torres, J. P. M. M. Rosa, G. P. Balthazar, D. Thomazini and M. V. Gelfuso, Microstructural evolution during sintering and thermoelectric characterization of La^{3+} and/or Nb^{5+} doped $CaMnO_3$ perovskites, *Ceram. Int.*, 2025, **51**(19), 27350–27362, DOI: 10.1016/j.ceramint.2025.03.409.

17 P. Amirkhizi, M. A. Madre, O. J. Dura, M. A. Torres, A. Sotelo, A. V. Kovalevsky, *et al.*, Enhancing thermoelectric performance of $CaMnO_3$ through a Y- and La- dual-doping strategy, *Ceram. Int.*, 2025, **51**(7), 9421–9428, DOI: 10.1016/j.ceramint.2024.12.375.

18 K. Park, D. H. Kim, S. Y. Gwon and E. C. Jeon, High thermoelectric performance of n–type $SrTiO_3$ by Dy and Nb co–doping, *Inorg. Chem. Commun.*, 2024, **169**, 113041, DOI: 10.1016/j.inoche.2024.113041.

19 H. Wu, X. L. Shi, W. D. Liu, M. Li, H. Gao, W. Zhou, *et al.*, Double perovskite Pr_2CoFeO_6 thermoelectric oxide: Roles of Sr-doping and Micro/nanostructuring, *Chem. Eng. J.*, 2021, **425**, 130668, DOI: 10.1016/j.cej.2021.130668.

20 L. Zhang, Z. Cao, Q. Q. Fu, C. Y. Li, Y. Q. Du, Y. N. Li, *et al.*, Thermoelectric properties of Yb-La-Nb-doped $SrTiO_3$, *J. Eur. Ceram. Soc.*, 2024, **44**(3), 1647–1653, DOI: 10.1016/j.jeurceramsoc.2023.10.028.

21 S. Z. A. Shah, S. Niaz, M. M. Alghamdi, A. A. El-Zahhar and A. Parveen, Bismuth doping enhances the stability, safety and efficiency of the double perovskite $Cs_2AgScBr_6$: A first-principles journey toward high performance, *Int. J. Mod. Phys. B*, 2026, **40**(5), 2650042, DOI: 10.1142/S0217979226500426.

22 S. Firdous, G. F. A. Malik, I. K. Pandey and F. A. Khanday, Investigation of optical properties of La_2NiMn0_6 *via* A-site doping with strontium and europium: A first-principle study, *J. Mater. Sci.: Mater. Electron.*, 2025, **36**(26), 1684, DOI: 10.1007/s10854-025-15754-3.

23 H. Jung, Z. Liu, M. Sotome, K. Nonomura, H. Segawa, G. Kapil, *et al.*, Improved Efficiency and Stability in Inverted-Structure Solar Cells with Lead-Free All-Inorganic Halide Perovskite $CsSn_{1-x}Zn_xBr_3$, *ACS Appl. Mater. Interfaces*, 2025, **17**(10), 15613–15620, DOI: 10.1021/acsami.4c21442.

24 D. Gahlawat, J. Kaur, R. Basu, A. K. Sharma, U. Rani, J. Madan, *et al.*, Theoretical and Numerical Insights into $Ba(Hf_{1-x}Zr_x)S_3$ Perovskites: Bandgap Tuning and Device-Level Simulation for Efficient Solar Cells, *ACS Appl. Opt. Mater.*, 2025, **3**(9), 2129–2152, DOI: 10.1021/acsaom.5c00267.

25 A. Hossain, M. M. Haque, A. Hayitov, A. I. Ashirova, S. S. Mahtab, S. Homyra, *et al.*, Sulfur substitution in $BaZrO_3$ perovskite: A first-principles study of bandgap tuning for photovoltaic applications, *AIP Adv.*, 2026, **16**(1), 015018, DOI: 10.1063/5.0312419.

26 Y. Huang, X. Wang, X. Li, Z. Liu, F. Wang, W. Yu, *et al.*, Doping effect on the electronic and optical properties of all-inorganic $CsGeBr_{3-x}I_x$, *Opt. Express*, 2026, **34**(2), 2744, DOI: 10.1364/OE.582440.

27 W. L. Leal Filho, R. Kotter, P. G. Özuyar, I. R. Abubakar, J. H. P. P. Eustachio and N. R. Matandirotya, Understanding Rare Earth Elements as Critical Raw Materials, *Sustainability*, 2023, **15**(3), 1919, DOI: 10.3390/su15031919.

28 A. Khan, H. Al Rashid, P. K. Roy, S. I. Chowdhury and S. A. Sathi, Challenges and the Way to Improve Lithium-Ion Battery Technology for Next-Generation Energy Storage, *Energy Environ. Mater.*, 2025, **8**(6), e70088, DOI: 10.1002/eem2.70088.

29 V. V. Satya Prasad, R. G. Baligidad and A. A. Gokhale. in *Niobium and Other High Temperature Refractory Metals for*

Aerospace Applications, 2017. pp. 267–288. DOI: 10.1007/978-981-10-2134-3_12.

30 X. L. Shi, H. Wu, Q. Liu, W. Zhou, S. Lu, Z. Shao, *et al.*, $SrTiO_3$-based thermoelectrics: Progress and challenges, *Nano Energy*, 2020, **78**, 105195, DOI: 10.1016/j.nanoen.2020.105195.

31 C. Feldmann and M. Jansen, Zur kristallchemischen Ähnlichkeit von Aurid- und Halogenid-Ionen, *Z. Anorg. Allg. Chem.*, 1995, **621**(11), 1907–1912, DOI: 10.1002/zaac.19956211113.

32 H. Sahrowsky, P. Vogt, K. Hippler and S. Sitla, Crystal structure of K_3OI, *Z. Kristallogr. - Cryst. Mater.*, 1991, **196**(1–4), 193–196, DOI: 10.1524/zkri.1991.196.14.193.

33 K. Kim, Y. Li, P. C. Tsai, F. Wang, S. B. Son, Y. M. Chiang, *et al.*, Exploring the Synthesis of Alkali Metal Anti-perovskites, *Chem. Mater.*, 2022, **34**(3), 947–958, DOI: 10.1021/acs.chemmater.1c02150.

34 P. Giannozzi, S. Baroni, N. Bonini, M. Calandra, R. Car, C. Cavazzoni, *et al.*, QUANTUM ESPRESSO: a modular and open-source software project for quantum simulations of materials, *J. Phys.: Condens. Matter*, 2009, **21**(39), 395502, DOI: 10.1088/0953-8984/21/39/395502.

35 A. Dal Corso, Pseudopotentials periodic table: From H to Pu, *Comput. Mater. Sci.*, 2014, **95**, 337–350, DOI: 10.1016/j.commatsci.2014.07.043.

36 M. De La Pierre, R. Orlando, L. Maschio, K. Doll, P. Ugliengo and R. Dovesi, Performance of six functionals (LDA, PBE, PBESOL, B3LYP, PBE0, and WC1LYP) in the simulation of vibrational and dielectric properties of crystalline compounds. The case of forsterite Mg_2SiO_4, *J. Comput. Chem.*, 2011, **32**(9), 1775–1784, DOI: 10.1002/jcc.21750.

37 P. Ziesche, S. Kurth and J. P. Perdew, Density functionals from LDA to GGA, *Comput. Mater. Sci.*, 1998, **11**(2), 122–127, DOI: 10.1016/S0927-0256(97)00206-1.

38 B. Hammer, L. B. Hansen and J. K. Nørskov, Improved adsorption energetics within density-functional theory using revised Perdew-Burke-Ernzerhof functionals, *Phys. Rev. B*, 1999, **59**(11), 7413–7421, DOI: 10.1103/PhysRevB.59.7413.

39 J. Heyd, G. E. Scuseria and M. Ernzerhof, Hybrid functionals based on a screened Coulomb potential, *J. Chem. Phys.*, 2003, **118**(18), 8207–8215, DOI: 10.1063/1.1564060.

40 F. Birch, Finite Elastic Strain of Cubic Crystals, *Phys. Rev.*, 1947, **71**(11), 809–824, DOI: 10.1103/PhysRev.71.809.

41 F. D. Murnaghan, The Compressibility of Media under Extreme Pressures, *Proc. Natl. Acad. Sci. U. S. A.*, 1944, **30**(9), 244–247, DOI: 10.1073/pnas.30.9.244.

42 K. Momma and F. Izumi, VESTA 3 for three-dimensional visualization of crystal, volumetric and morphology data, *J. Appl. Crystallogr.*, 2011, **44**(6), 1272–1276, DOI: 10.1107/S0021889811038970.

43 M. W. Qureshi, X. Ma, G. Tang and R. Paudel, Ab initio predictions of structure and physical properties of the Zr_2GaC and Hf_2GaC MAX phases under pressure, *Sci. Rep.*, 2021, **11**(1), 3260, DOI: 10.1038/s41598-021-82402-1.

44 P. Giannozzi and S. Baroni. Density-Functional Perturbation Theory. in *Handbook of Materials Modeling*. Dordrecht: Springer Netherlands; 2005. pp. 195–214. DOI: 10.1007/978-1-4020-3286-8_11.

45 F. Knoop, N. Shulumba, A. Castellano, J. P. A. Batista, R. Farris, M. J. Verstraete, *et al.*, TDEP: Temperature Dependent Effective Potentials, *J. Open Source Softw.*, 2024, **9**(94), 6150, DOI: 10.21105/joss.06150.

46 J. Meller. Molecular Dynamics. in *Encyclopedia of Life Sciences*, Wiley; 2001. DOI: 10.1038/npg.els.0003048.

47 *Andrea Dal Corso*. https://dalcorso.github.io/thermo_pw/. Welcome to Thermo_pw Thermo_pw is a driver of quantum-ESPRESSO routines for the automatic computation of ab-initio material properties.

48 A. Otero-de-la-Roza and V. Luaña, Gibbs2: A new version of the quasi-harmonic model code. I. Robust treatment of the static data, *Comput. Phys. Commun.*, 2011, **182**(8), 1708–1720, DOI: 10.1016/j.cpc.2011.04.016.

49 G. K. H. Madsen and D. J. Singh, BoltzTraP. A code for calculating band-structure dependent quantities, *Comput. Phys. Commun.*, 2006, **175**(1), 67–71, DOI: 10.1016/j.cpc.2006.03.007.

50 C. J. Bartel, C. Sutton, B. R. Goldsmith, R. Ouyang, C. B. Musgrave, L. M. Ghiringhelli, *et al.*, New tolerance factor to predict the stability of perovskite oxides and halides, *Sci. Adv.*, 2019, **5**(2), eaav0693, DOI: 10.1126/sciadv.aav0693.

51 Y. Zhao and K. Zhu, Organic–inorganic hybrid lead halide perovskites for optoelectronic and electronic applications, *Chem. Soc. Rev.*, 2016, **45**(3), 655–689, DOI: 10.1039/C4CS00458B.

52 Q. Q. Liang, D. Y. Hu, T. Y. Tang, H. X. Gao, S. Q. Wu, L. Li, *et al.*, First-principles calculations to investigate structural, electronic, optical and thermodynamic properties of anti-perovskite compounds X_3OI(X = Na, K, Rb), *J. Mater. Res. Technol.*, 2023, **22**, 3245–3254, DOI: 10.1016/j.jmrt.2022.12.148.

53 H. Xiao, T. Hu, P. Zhou and D. Li, First-principles investigations on the thermal transport and thermoelectric properties of anti-perovskite M_3OI and M_4OI_2 (M = K, Rb), *Front Phys*, 2025, **13**, 1619661, DOI: 10.3389/fphy.2025.1619661.

54 R. N. Mondal, F. T. Zahra, MdB. H. Parosh and MdS. N. Romel, Unveiling Thermal, Phonon, and Optoelectronic Characteristics of Cs_3O X (X = Cl, Br, or I) Antiperovskites for Sustainable Energy Applications: A DFT Exploration, *Int. J. Energy Res.*, 2026, **2026**(1), 5561106, DOI: 10.1155/er/5561106.

55 S. H. Ri, U. G. Jong, T. S. Im and U. R. Rim, Perovskite-type hydrides $ACaH_3$ (A = Li, Na): computational investigation on materials properties for hydrogen storage applications, *RSC Adv.*, 2025, **15**(24), 19245–19253, DOI: 10.1039/D5RA01810B.

56 K. Tolborg and A. Walsh, Exploring the High-Temperature Stabilization of Cubic Zirconia from Anharmonic Lattice Dynamics, *Cryst. Growth Des.*, 2023, **23**(5), 3314–3319, DOI: 10.1021/acs.cgd.2c01458.

57 A. Ramzan, M. Y. Sofi, M. Ishfaq-ul-Islam, M. S. Khan and M. A. Khan, Half-metallic ferromagnetism and thermoelectric-efficient behavior in chalcogenide spinels $MgNi_2X_4$ (X = S, Se): a first-principles approach, *RSC Adv.*, 2025, **15**(29), 24002–24018, DOI: 10.1039/D5RA03555D.

58 T. Das, G. Di Liberto and G. Pacchioni, Density Functional Theory Estimate of Halide Perovskite Band Gap: When Spin Orbit Coupling Helps, *J. Phys. Chem. C*, 2022, **126**(4), 2184–2198, DOI: 10.1021/acs.jpcc.1c09594.

59 Y. K. Jung, J. H. Lee, A. Walsh and A. Soon, Influence of Rb/Cs Cation-Exchange on Inorganic Sn Halide Perovskites: From Chemical Structure to Physical Properties, *Chem. Mater.*, 2017, **29**(7), 3181–3188, DOI: 10.1021/acs.chemmater.7b00260.

60 F. Benlakhdar, M. A. Ghebouli, M. Fatmi, B. Ghebouli, S. Alomairy, M. J. A. Abualreish, *et al.*, Electronic and optical properties of lead-free $K_2AgSbBr_6$ double perovskite tuned by doping elements Cu^+, Bi^{3+}, and I^-, *Sci. Rep.*, 2025, **15**(1), 40362, DOI: 10.1038/s41598-025-24417-6.

61 T. He, L. Chen, Y. Su, Y. Lu, L. Bao, G. Chen, *et al.*, The effects of alkali metal ions with different ionic radii substituting in Li sites on the electrochemical properties of Ni-Rich cathode materials, *J. Power Sources*, 2019, **441**, 227195, DOI: 10.1016/j.jpowsour.2019.227195.

62 T. Sandu and R. I. Iftimie, Bandgaps and band bowing in semiconductor alloys, *Solid State Commun.*, 2010, **150**(17–18), 888–892, DOI: 10.1016/j.ssc.2010.01.046.

63 G. Orsal, Y. El Gmili, N. Fressengeas, J. Streque, R. Djerboub, T. Moudakir, *et al.*, Bandgap energy bowing parameter of strained and relaxed InGaN layers, *Opt. Mater. Express*, 2014, **4**(5), 1030, DOI: 10.1364/OME.4.001030.

64 Y. Koide, H. Itoh, M. R. H. Khan, K. Hiramatu, N. Sawaki and I. Akasaki, Energy band-gap bowing parameter in an $Al_xGa_{1-x}N$ alloy, *J. Appl. Phys.*, 1987, **61**(9), 4540–4543, DOI: 10.1063/1.338387.

65 B. Ehrler, E. Alarcón-Lladó, S. W. Tabernig, T. Veeken, E. C. Garnett and A. Polman, Photovoltaics Reaching for the Shockley–Queisser Limit, *ACS Energy Lett.*, 2020, **5**(9), 3029–3033, DOI: 10.1021/acsenergylett.0c01790.

66 W. Shockley and H. J. Queisser, Detailed Balance Limit of Efficiency of p–n Junction Solar Cells, *J. Appl. Phys.*, 1961, **32**(3), 510–519, DOI: 10.1063/1.1736034.

67 X. H. Yang, Enhancing thermoelectric properties of semiconductors by heavily doping isoelectronic elements with electronegativities distinct from the host atoms, *J. Alloys Compd.*, 2014, **594**, 70–75, DOI: 10.1016/J.JALLCOM.2014.01.070.

68 W. S. Yun, J. S. Kim and M. J. Lee, High p-type thermoelectric performance driven by a nearly flat band in single-layer $CdSbS_3$, *Dalton Trans.*, 2025, **54**(47), 17546–17552, DOI: 10.1039/D5DT02632F.

69 M. A. Ghebouli, K. Bouferrache, F. K. Alanazi, B. Ghebouli and M. Fatmi, Stability, mechanical, optoelectronic and thermoelectric behaviors of inorganic metal halide double perovskites $(Cs_2, K_2, Rb_2)SnCl_6$: Promising green energy alternatives, *Solid State Commun.*, 2025, **397**, 115831, DOI: 10.1016/j.ssc.2025.115831.

70 M. Yu, W. Gao, X. Shi, Q. Yuan, B. Wang, L. Ju, *et al.*, Polar iodate $BiO(IO_3)$: A two-dimensional ultrawide-bandgap semiconductor with high carrier mobility and robust piezoelectricity, *Results Phys*, 2024, **59**, 107561, DOI: 10.1016/j.rinp.2024.107561.

71 S. Zhang, M. C. Tang, Y. Fan, R. Li, N. V. Nguyen, K. Zhao, *et al.*, Role of Alkali-Metal Cations in Electronic Structure and Halide Segregation of Hybrid Perovskites, *ACS Appl. Mater. Interfaces*, 2020, **12**(30), 34402–34412, DOI: 10.1021/acsami.0c08396.

72 F. Mouhat and F. X. Coudert, Necessary and sufficient elastic stability conditions in various crystal systems, *Phys. Rev. B*, 2014, **90**(22), 224104, DOI: 10.1103/PhysRevB.90.224104.

73 MdA. Sarker, M. M. Hasan, Md Al Momin, A. Irfan, MdR. Islam and A. Sharif, Band gap engineering in lead free halide cubic perovskites $GaGeX_3$ (X = Cl, Br, and I) based on first-principles calculations, *RSC Adv.*, 2024, **14**(14), 9805–9818, DOI: 10.1039/D4RA00224E.

74 S. H. Jhi, J. Ihm, S. G. Louie and M. L. Cohen, Electronic mechanism of hardness enhancement in transition-metal carbonitrides, *Nature*, 1999, **399**(6732), 132–134, DOI: 10.1038/20148.

75 A. I. Lurie and A. Belyaev. *Theory of Elasticity*. Berlin, Heidelberg: Springer Berlin Heidelberg; 2005. DOI: 10.1007/978-3-540-26455-2.

76 S. F. Pugh, XCII. Relations between the elastic moduli and the plastic properties of polycrystalline pure metals, *London, Edinburgh Dublin Philos. Mag. J. Sci.*, 1954, **45**(367), 823–843, DOI: 10.1080/14786440808520496.

77 J. Wang, Y. Lu and X. Shao, First-Principles Calculation for the Influence of C and O on the Mechanical Properties of γ-TiAl Alloy at High Temperature, *Metals*, 2019, **9**(2), 262, DOI: 10.3390/met9020262.

78 D. Music, Z. Sun, R. Ahuja and J. M. Schneider, Electronic structure of $M_2AlC(0001)$ surfaces (M = Ti,V,Cr), *J. Phys.: Condens. Matter*, 2006, **18**(39), 8877–8881, DOI: 10.1088/0953-8984/18/39/017.

79 S. I. Ranganathan and M. Ostoja-Starzewski, Universal Elastic Anisotropy Index, *Phys. Rev. Lett.*, 2008, **101**(5), 055504, DOI: 10.1103/PhysRevLett.101.055504.

80 K. Yuan, X. Zhang, Y. Gao and D. Tang, Soft phonon modes lead to suppressed thermal conductivity in Ag-based chalcopyrites under high pressure, *Phys. Chem. Chem. Phys.*, 2023, **25**(36), 24883–24893, DOI: 10.1039/D3CP03087C.

81 M. W. Qureshi, M. A. Ali and X. Ma, Screen the thermomechanical and optical properties of the new ductile 314 MAX phase boride Zr_3CdB_4: A DFT insight, *J. Alloys Compd.*, 2021, **877**, 160248, DOI: 10.1016/j.jallcom.2021.160248.

82 R. M. Atikur, M. Hasan, J. F. Lubna, R. Khatun, S. Sarker, M. Z. Hasan, *et al.*, Comparative study of the structural, mechanical, electronic, optical and thermodynamic properties of superconducting disilicide YT_2Si_2 (T=Co, Ni,

Ru, Rh, Pd, Ir) by DFT simulation, *J. Phys. Chem. Solids*, 2023, **178**, 111342, DOI: 10.1016/j.jpcs.2023.111342.

83 O. L. Anderson, A simplified method for calculating the debye temperature from elastic constants, *J. Phys. Chem. Solids*, 1963, **24**(7), 909–917, DOI: 10.1016/0022-3697(63)90067-2.

84 P. R. Pansara, U. M. Meshiya, A. R. Makadiya, P. Y. Raval, K. B. Modi and P. M. G. Nambissan, Defect structure transformation during substitution in quadruple perovskite $CaCu_3$-Ti_4-Fe_2O_{12} studied by positron annihilation spectroscopy, *Ceram. Int.*, 2019, **45**(15), 18599–18603, DOI: 10.1016/j.ceramint.2019.06.083.

85 Y. Zhu, B. Wei, J. Liu, N. Z. Koocher, Y. Li, L. Hu, *et al.*, Physical insights on the low lattice thermal conductivity of $AgInSe_2$, *Mater. Today Phys.*, 2021, **19**, 100428, DOI: 10.1016/j.mtphys.2021.100428.

86 M. E. Fine, L. D. Brown and H. L. Marcus, Elastic constants *versus* melting temperature in metals, *Scr. Metall.*, 1984, **18**(9), 951–956, DOI: 10.1016/0036-9748(84)90267-9.

87 A. I. Lebedev, Ferroelectric properties of $RbNbO_3$ and $RbTaO_3$, *Phys. Solid State*, 2015, **57**(2), 331–336, DOI: 10.1134/S1063783415020237.

88 Z. Ali, I. Khan, I. Ahmad, M. S. Khan and S. J. Asadabadi, Theoretical studies of the paramagnetic perovskites $MTaO_3$ (M = Ca, Sr and Ba), *Mater. Chem. Phys.*, 2015, **162**, 308–315, DOI: 10.1016/j.matchemphys.2015.05.072.

89 M. A. Blanco, E. Francisco and V. Luaña, GIBBS: isothermal-isobaric thermodynamics of solids from energy curves using a quasi-harmonic Debye model, *Comput. Phys. Commun.*, 2004, **158**(1), 57–72, DOI: 10.1016/j.comphy.2003.12.001.

90 M. Sarwan, V. A. Shukoor, M. F. Shareef and S. Singh, A first principle study of structural, elastic, electronic and thermodynamic properties of Half-Heusler compounds; YNiPn (Pn=As, sb, and bi), *Solid State Sci.*, 2021, **112**, 106507, DOI: 10.1016/j.solidstatesciences.2020.106507.

91 D. C. Jiles, *Introduction to the Electronic Properties of Materials*, CRC Press, 2001, DOI: 10.1201/9781315273365.

92 S. A. Holgate. *Understanding Solid State Physics*. CRC Press, 2009. DOI: 10.1201/b15977.

93 N. Louati, F. Oumelaz, O. Nemiri, D. Boudjaadar, A. Boumaza, R. Benredouane, *et al.*, Investigation of Structural, Optoelectronic, Thermoelectric, and Elastic Properties for Sr_2NaXO_6 (X = Cl, Br, and I) Advanced Double Perovskite Semiconductors: *Ab Initio* Study, *Phys. Status Solidi B*, 2025, **262**(6), 2400677, DOI: 10.1002/pssb.202400677.

94 M. A. Green, Y. Jiang, A. M. Soufiani and A. Ho-Baillie, Optical Properties of Photovoltaic Organic–Inorganic Lead Halide Perovskites, *J. Phys. Chem. Lett.*, 2015, **6**(23), 4774–4785, DOI: 10.1021/acs.jpclett.5b01865.

95 S. Berri, Ab-initio calculations on structural, electronic, half-metallic and optical properties of Co-, Fe-, Mn- and Cr-doped Ba_2LuTaO_6, *Pramana*, 2021, **95**(1), 38, DOI: 10.1007/s12043-020-02026-4.

96 R. A. S. Md Sayem and K. M. Shorowordi, First-principles study of novel non-toxic trigonal $KGeX_3$ (X=Br, I) perovskites: A potential for optoelectronic applications, *Mater. Sci. Semicond. Process.*, 2025, **186**, 109114, DOI: 10.1016/j.mssp.2024.109114.

97 MdS. Alam, M. Saiduzzaman, A. Biswas, T. Ahmed, A. Sultana and K. M. Hossain, Tuning band gap and enhancing optical functions of $AGeF_3$ (A = K, Rb) under pressure for improved optoelectronic applications, *Sci. Rep.*, 2022, **12**(1), 8663, DOI: 10.1038/s41598-022-12713-4.

98 U. Ahmed, H. Akter, A. Hossain, M. M. Hossian, M. M. Uddin, S. H. Naqib, *et al.*, Anion (S) substitution as a pathway for tuning the physical properties of $CsTaO_3$, *New J. Chem.*, 2025, **49**(18), 7682–7699, DOI: 10.1039/D5NJ00025D.

99 C. J. Yu, I. C. Ri, H. M. Ri, J. H. Jang, Y. S. Kim and U. G. Jong, First-principles study on structural, electronic and optical properties of halide double perovskite Cs_2AgBX_6 (B = In, Sb; X = F, Cl, Br, I), *RSC Adv.*, 2023, **13**(23), 16012–16022, DOI: 10.1039/D3RA02566G.

100 S. Mahmud, U. Ahmed, MdA. U. Z. Atik, MdM. Hossain, MdM. Uddin and MdA. Ali, Novel $Cs_2Au^{I}M^{III}F_6$ (M = As, Sb) double halide perovskites: sunlight and industrial waste heat management device applications, *Phys. Chem. Chem. Phys.*, 2025, **27**(9), 4686–4703, DOI: 10.1039/D4CP04293J.

101 T. J. Scheidemantel, C. Ambrosch-Draxl, T. Thonhauser, J. V. Badding and J. O. Sofo, Transport coefficients from first-principles calculations, *Phys. Rev. B*, 2003, **68**(12), 125210, DOI: 10.1103/PhysRevB.68.125210.

102 G. A. Slack, Nonmetallic crystals with high thermal conductivity, *J. Phys. Chem. Solids*, 1973, **34**(2), 321–335, DOI: 10.1016/0022-3697(73)90092-9.

103 T. Feng and X. Ruan, Quantum mechanical prediction of four-phonon scattering rates and reduced thermal conductivity of solids, *Phys. Rev. B*, 2016, **93**(4), 045202, DOI: 10.1103/PhysRevB.93.045202.

104 K. Zhao, M. Li, H. Wuliji, H. Gao, H. Chen, P. Qiu, *et al.*, Strong Lattice Softening Induced by Atomic Mismatch in Meta-Phase Thermoelectrics, *Advanced Science*, 2025, **12**(48), e14105, DOI: 10.1002/advs.202514105.

105 H. Xie, S. Hao, J. Bao, T. J. Slade, G. J. Snyder, C. Wolverton, *et al.*, All-Inorganic Halide Perovskites as Potential Thermoelectric Materials: Dynamic Cation off-Centering Induces Ultralow Thermal Conductivity, *J. Am. Chem. Soc.*, 2020, **142**(20), 9553–9563, DOI: 10.1021/jacs.0c03427.

106 M. Y. Sofi, M. S. Khan and M. A. Khan, Control of spin on ferromagnetism and thermoelectric properties of K_2GeMnX_6 (X = Cl, Br, I) halide perovskites: emerging candidates for semiconductor spintronics and thermoelectric applications, *Mater. Adv.*, 2024, **5**(11), 4913–4931, DOI: 10.1039/D3MA01160G.

107 K. P. Mishra and B. K. Pandey, Simulation-driven materials engineering of $CsBX_3$ perovskite solar cells for enhanced operational stability, *Renewable Energy*, 2026, **256**, 124007, DOI: 10.1016/j.renene.2025.124007.

108 F. J. DiSalvo, Thermoelectric Cooling and Power Generation, *Science*, 1999, **285**(5428), 703–706, DOI: 10.1126/science.285.5428.703.

109 J. Qiu, S. Zhi, P. Zhao, J. Wang, X. Ma, S. Ye, *et al.*, Revealing the significant role of band structure asymmetry on thermoelectric bipolar conduction, *Phys. Rev. B*, 2025, **111**(4), 045203, DOI: 10.1103/PhysRevB.111.045203.

110 U. G. Jong, Y. S. Kim, C. H. Ri, Y. H. Kye and C. J. Yu, High Thermoelectric Performance in the Cubic Inorganic Cesium Iodide Perovskites $CsBI_3$ (B = Pb, Sn, and Ge) from First-Principles, *J. Phys. Chem. C*, 2021, **125**(11), 6013–6019, DOI: 10.1021/acs.jpcc.0c09929.

111 A. Z. Khan, J. M. Flitcroft and J. M. Skelton, First-principles modelling of the thermoelectric properties of n-type $CaTiO_3$, $SrTiO_3$ and $BaTiO_3$, *Mater. Adv.*, 2024, **5**(2), 652–664, DOI: 10.1039/D3MA00624G.

112 S. Tinte, M. G. Stachiotti, M. Sepliarsky, R. L. Migoni and C. O. Rodriguez, Atomistic modelling of $BaTiO_3$ based on first-principles calculations, *J. Phys.: Condens. Matter*, 1999, **11**(48), 9679–9690, DOI: 10.1088/0953-8984/11/48/325.

113 T. TADANO and S. TSUNEYUKI, Ab initio prediction of structural phase-transition temperature of $SrTiO_3$ from finite-temperature phonon calculation, *J. Ceram. Soc. Jpn.*, 2019, **127**(6), 404–408, DOI: 10.2109/jcersj2.18216.

114 I. Maeng, S. Lee, H. Tanaka, J. H. Yun, S. Wang, M. Nakamura, *et al.*, Unique phonon modes of a $CH_3NH_3PbBr_3$ hybrid perovskite film without the influence of defect structures: an attempt toward a novel THz-based application, *NPG Asia Mater.*, 2020, **12**(1), 53, DOI: 10.1038/s41427-020-0235-6.